SIMULATION OF THE FAST FLUX TEST FACILITY LOSS-OF-FLOW WITHOUT SCRAM ACCIDENT SCENARIO USING THE SAM COMPUTER CODE

A Thesis

by

BRENT PATRICK HOLLRAH

Submitted to the Office of Graduate and Professional Studies of
Texas A&M University
in partial fulfillment of the requirements for the degree of

MASTER OF SCIENCE

Chair of Committee,	Yassin A. Hassan
Co-Chair of Committee,	Rodolfo Vaghetto
Committee Member,	Victor M. Ugaz
Head of Department,	Michael Nastasi

December 2020

Major Subject: Nuclear Engineering

ABSTRACT

A major appeal of sodium fast reactors is their passive safety capabilities. To demonstrate this, a series of Loss of Flow WithOut Scram (LOFWOS) tests were conducted at the Fast Flux Test Facility (FFTF) under different reactor power levels. Experimental results from this test were made available through IAEA CRP I32011 for use in a code benchmarking activity. In this work, the System Analysis Module (SAM) was used to analyze the response of the FFTF during one of the LOFWOS transients (Test #13). Efforts were made first to develop a faithful representation of the facility and its main components and control systems. The model was used to predict the steady-state conditions of the plant. The results were compared with provided experimental data, confirming the predictions to be in overall satisfactory agreement. Flow rates and pump head were matched to experimental values within 0.2% in each loop. Additionally, the core inlet temperature was matched within 0.2%. The validated SAM model was then used to predict the thermal-hydraulic response of the system during the first 900 seconds after the initiation of the LOFWOS transient. Selected parameters of interest (system mass flow rate, select core assembly outlet temperatures, primary loop hot and cold leg temperatures, and fission power) were compared to experimental results, revealed at the end of the blind phase of the benchmark activity. The results of the first phase of this benchmark exercise were promising, confirming the ability of the SAM code and the adequacy of the model to capture the general trend of the physical phenomena observed during the transient. Deviations from the experimental results were also identified. An

additional SAM simulation was executed using updated boundary conditions taken from the experimental results to further improve the overall predictions and agreement with the experimental results.

ACKNOWLEDGEMENTS

I would like to thank my committee chair, Dr. Hassan, for first introducing me to the field of the nuclear engineering thermal hydraulics when I was given the chance to intern at the Texas A&M Thermal Hydraulics Research Laboratory as an undergraduate student. Thanks also to my committee co-chair Dr. Vaghetto for his continued guidance during this project and my time at Texas A&M in general. The support of Dr. Hassan and Dr. Vaghetto has been essential for my growth as a graduate student, and I'm looking forward to continuing to learn from them as I continue my education. I would also like to thank Dr. Ugaz for his role as a member of my committee.

I would also like to thank Dr. Rui Hu and Dr. Ling Zou of Argonne National Laboratory for the opportunities they have given me as a summer intern and beyond. Completing the work for this thesis would not have been possible without their role in teaching me to use and understand the SAM code.

Thanks also to everyone who made this benchmark a reality, including the organizers from the IAEA, Argonne National Laboratory, and Pacific Northwest National Laboratory. Special thanks to Dr. Tyler Sumner of Argonne National Laboratory for his help addressing many technical questions during this project.

I would also like to thank my colleagues and friends in the Texas A&M Thermal Hydraulics Research Laboratory. The sense of community provided by everyone who is a part of this lab has made my time at Texas A&M a truly memorable and worthwhile experience.

Finally, thank you to my mom, dad, sister, grandparents, and the rest of my family for the endless support and encouragement you have given me.

The data and information presented in the paper are part of an ongoing IAEA coordinated research project on “Benchmark Analysis of Fast Flux Test Facility (FFTF) Loss of Flow Without Scram Test – CRP-I32011”

CONTRIBUTORS AND FUNDING SOURCES

Contributors

This work was supervised by a thesis committee consisting of committee chair, Dr. Yassin Hassan, and committee co-chair, Dr. Rodolfo Vaghetto of the Department of Nuclear Engineering, and committee member Dr. Victor Ugaz of the Department of Chemical Engineering.

Funding Sources

Graduate study was supported by the Engineering Graduate Merit Fellowship in the Department of Nuclear Engineering

TABLE OF CONTENTS

Page

LIST OF FIGURES

Page

LIST OF TABLES

Page

1. INTRODUCTION

Nuclear power is an appealing source of energy thanks to its ability to meet baseload electricity demand without emitting greenhouse gasses and other pollutants into the atmosphere. Currently, the majority of reactors in the U.S. and worldwide are light water reactors (LWRs). While these designs have operated successfully for decades, they are facing increased economic pressure from natural gas and renewable energy sources. To meet challenges facing the current LWR fleet, the nuclear industry has invested in the next generation of nuclear power plants including sodium cooled fast reactors (SFRs). By using a fast neutron spectrum, SFRs can extract more energy per unit of fuel compared to LWRs. Fast reactors can also breed new fuel from existing reserves of low-enriched uranium or spent LWR fuel, potentially improving reactor economics. Waste produced by SFRs has more favorable characteristics than waste produced by LWRs, with shorter-lived isotopes. Using sodium as the coolant also has safety advantages including passive shutdown and passive decay heat removal capabilities.

With the goal of increasing global capabilities for modeling thermal hydraulic and neutronics effects in SFRs, the International Atomic Energy Agency organized a new Coordinated Research Project (CRP) I32011: Benchmark Analysis of FFTF Loss Of Flow Without Scram Test. This CRP is expected to have a range of benefits for the advancement of global SFR development including:

- Improving the understanding of loss of flow events in SFRs
- Validation of state-of-the-art analysis codes against experimental data

- Improving understanding of SFR neutronics, thermal-hydraulics, and system analysis
- Improving SFR simulation methodology
- Reducing uncertainty of SFR modeling codes
- Enhancing the reliability of predictions for future SFR designs
- Facilitating the training of the young generation of reactor physicists
- Identifying areas where additional research and development are required

In total, 26 organizations from 13 IAEA member states participated in the CRP [1].

This timeline for the CRP was divided into multiple phases. In the first phase, the blind phase, the CRP participants were provided a detailed description of the Fast Flux Test Facility (FFTF) to produce simulations of a loss of forced flow transient using the tools of their choice [2]. In this stage, the transient's experimental results were unavailable to participants. This provided an opportunity to assess and compare the effectiveness of the modeling strategies used by the participants. At the end of the blind phase, results were revealed to participants and the refined calculation phase began. In this phase, participants will evaluate their results to identify shortcomings in modeling strategies and code capabilities. When models are finalized at the end of the second phase, a third phase begins to qualify the differences between codes and modeling approaches. This phase will also include sensitivity analysis.

2. MOTIVATION AND OBJECTIVES

The motivation for participation in this CRP strongly overlaps with the IAEA's goals. The high quality experimental data made available for the benchmark is ideal to validate thermal hydraulic modeling tools on a SFR design with a transient including a range of complex phenomena that will be relevant to the design and licensing of future experimental and commercial SFR designs. A model that produces accurate results for the LOFWOS test can also be used as a predictive model to give insight into the impacts of other real and hypothetical transients.

The scope of this thesis primarily covers the blind phase of the CRP. The objectives of this phase are to create a model that is capable of producing an accurate model of the FFTF at the steady state initial conditions of the LOFWOS transient. This model will then be used to produce predictions of plant conditions during the LOFWOS transient. CRP participants were tasked with creating predictions for the following parameters to compare with experimental data collected during the test:

- Selected core assembly outlet temperatures
- Primary loop mass flow rates
- Primary loop hot leg temperatures
- Primary loop cold leg temperatures
- Fission power

This thesis also covers the analysis comparing the initial predictions with the experimental results. The experimental results were then used to update the boundary conditions of the model to better asses its strengths and weaknesses.

3. THE FAST FLUX TEST FACILITY

In an effort to advance SFR experience, perform materials and components testing, and demonstrate safety features, the FFTF was constructed at the US Department of Energy's (DoE) Hanford site in Washington State [2]. The FFTF first reached criticality in 1980 and was operated until 1993. Under normal operating conditions, the FFTF produced 400 MW_{th} and supported a total sodium flow rate of 2190 kg/s. The sodium coolant flowed from the reactor core to one of three primary coolant loops. Each loop contained a pump to drive the flow and an intermediate heat exchanger, which removed heat from the primary system to a secondary sodium loop. In the secondary loop, heat was removed from the system to the atmosphere via air-cooled dump heat exchangers. An overview of the FFTF coolant system is shown in Figure 1.

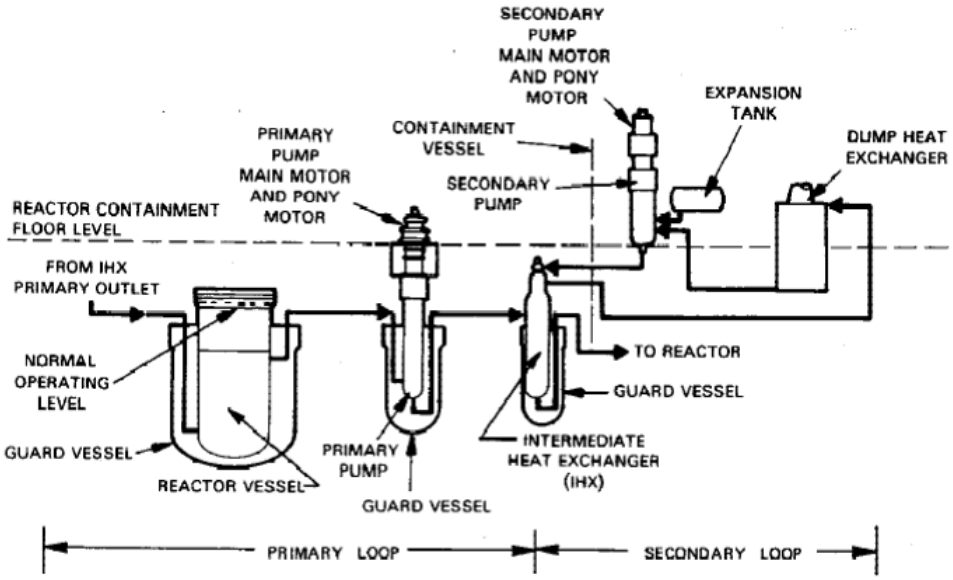

Figure 1. FTFF coolant system overview. Reprinted with permission. [2]

The core loading of the FFTF during the LOFOWS test is shown in Figure 2. This layout consisted of six inner rings of fueled assemblies, and three outer rings of reflector assemblies. The locations of control, safety, and test assemblies are also shown.

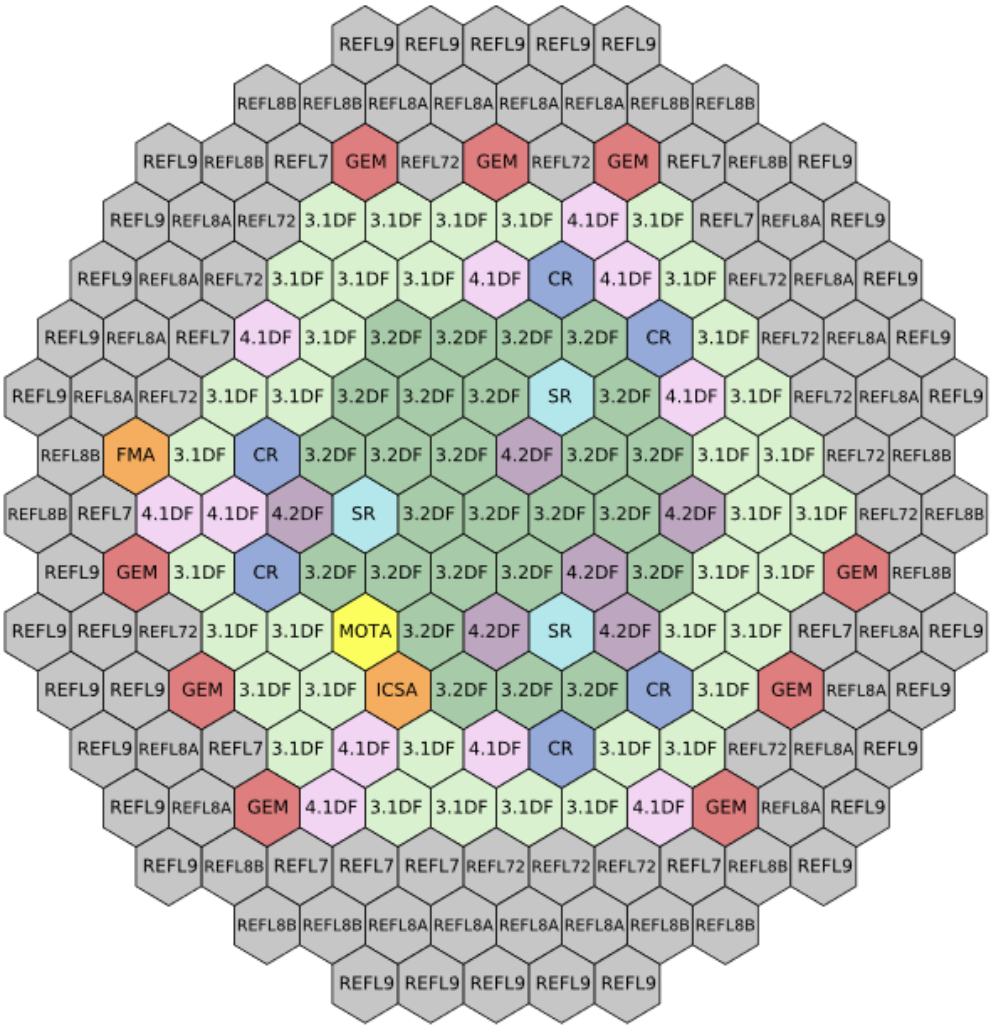

Figure 2. FFTF core layout. Reprinted with permission. [2]

A critical component of the reactor core was the Gas Expansion Modules (GEMs). The GEMs increased the passive shutdown capabilities of the core by increasing the neutron leakage from the core in the event of a pump depressurization. Each GEM was open to the sodium coolant at its lower end. The upper end contained a pocket of argon gas. During normal reactor operation, the pressure produced by the pump compressed the argon above the active region of the core. The sodium that filled the GEM increased the number of neutrons reflected back into the core, increasing the k_{eff} and allowing the reactor to go critical. In the event the GEMs are depressurized, as in the LOFWOS tests, the argon gas expands below the active region of the core, allowing more neutrons to leak from the core. This decreases the k_{eff} and, provided there are no overpowering positive feedback mechanisms, will allow the core to passively shut down.

The Reactor Vessel (RV), shown in Figure 3, contained the FFTF core and other components needed for proper shielding and cooling considerations. Coolant entered into the RV inlet plenum where it was divided to flow through the reactor core, radial shielding, core bypass, or in-vessel storage. Before exiting to the primary coolant loops, the coolant converged in the outlet plenum. An argon cover gas was maintained above the outlet plenum at a pressure of 102 kPa.

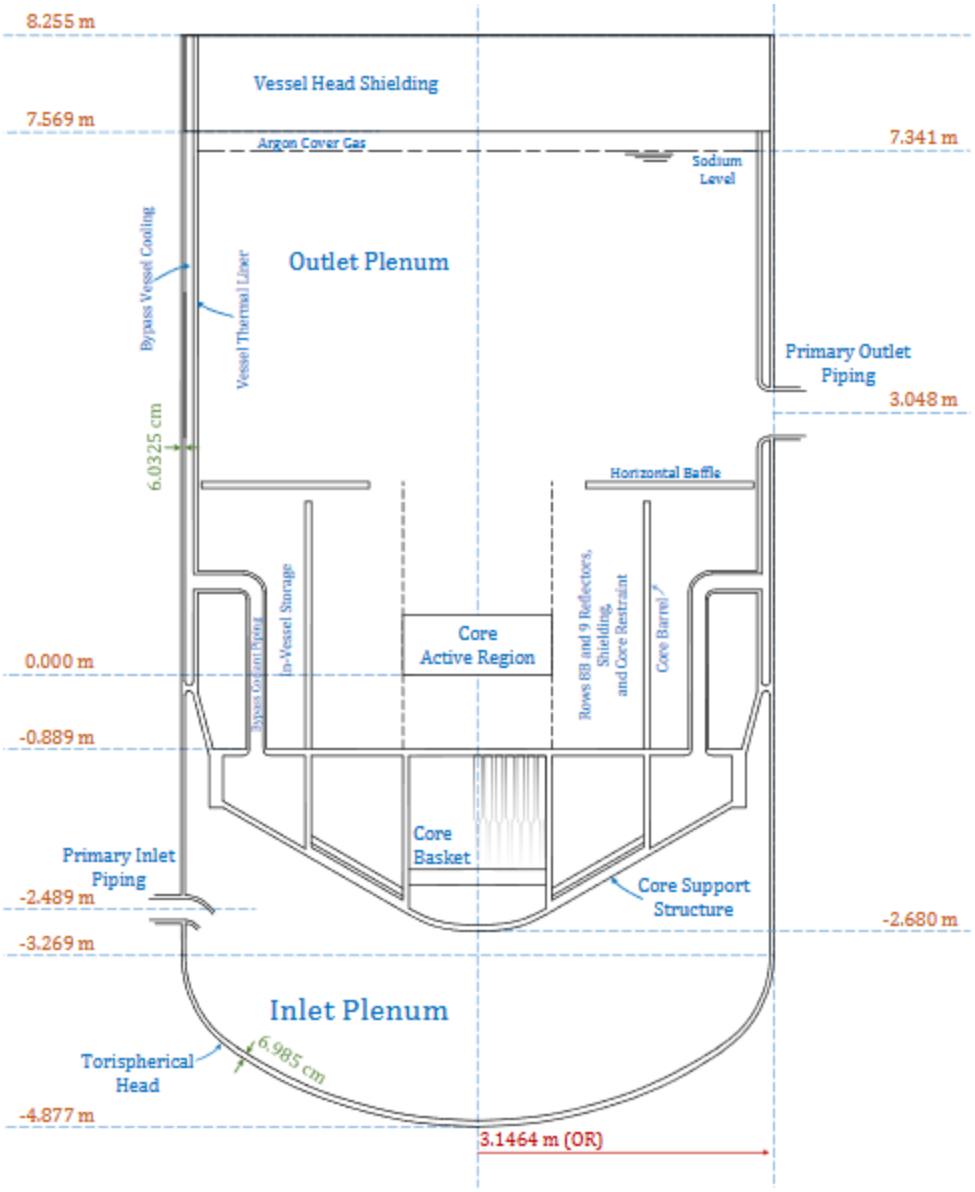

Figure 3. FFTF Reactor Vessel. Elevations relative to the core active region are shown in orange. Reprinted with permission. [2]

The FFTF contained three primary coolant loops, shown in Figure 4. Each loop consisted of a sodium pump, an intermediate heat exchanger (IHX), instrumentation to measure temperature and flow rates, and control valves. Each primary coolant loop had a

flow rate of roughly 734 kg/s. The IHX, shown in Figure 5, was a significant component for the passive safety of the FFTF. The IHX had a vertically mounted, counterflow, shell and tube design. The coolant in the primary loop flowed through the shell side of the IHX and the secondary coolant flowed through the tube side. Crucially, each IHX was located above the active region of the core. By cooling the sodium at a higher elevation from where it is heated, the change in density associated with the temperature changes can be utilized to drive a natural circulation flow. This feature allowed the reactor to passively remove decay heat from the core in the case of a loss of forced flow accident.

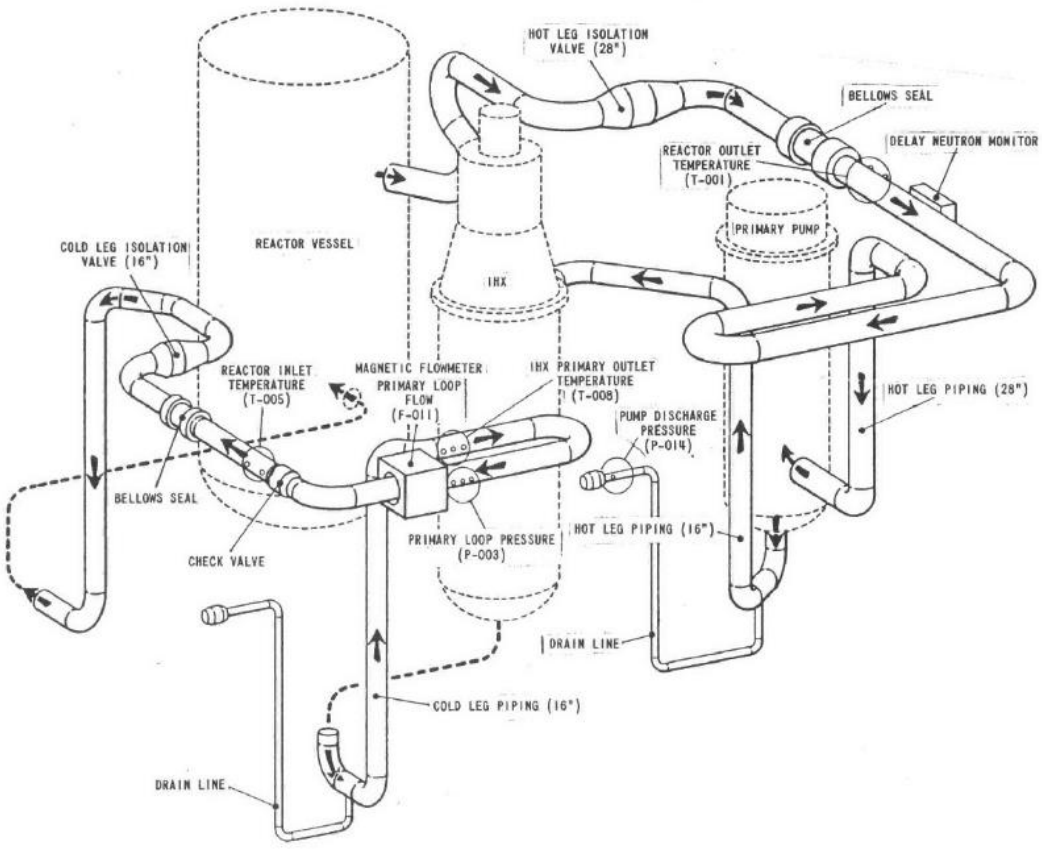

Figure 4. FFTF primary coolant loops. Reprinted with permission. [2]

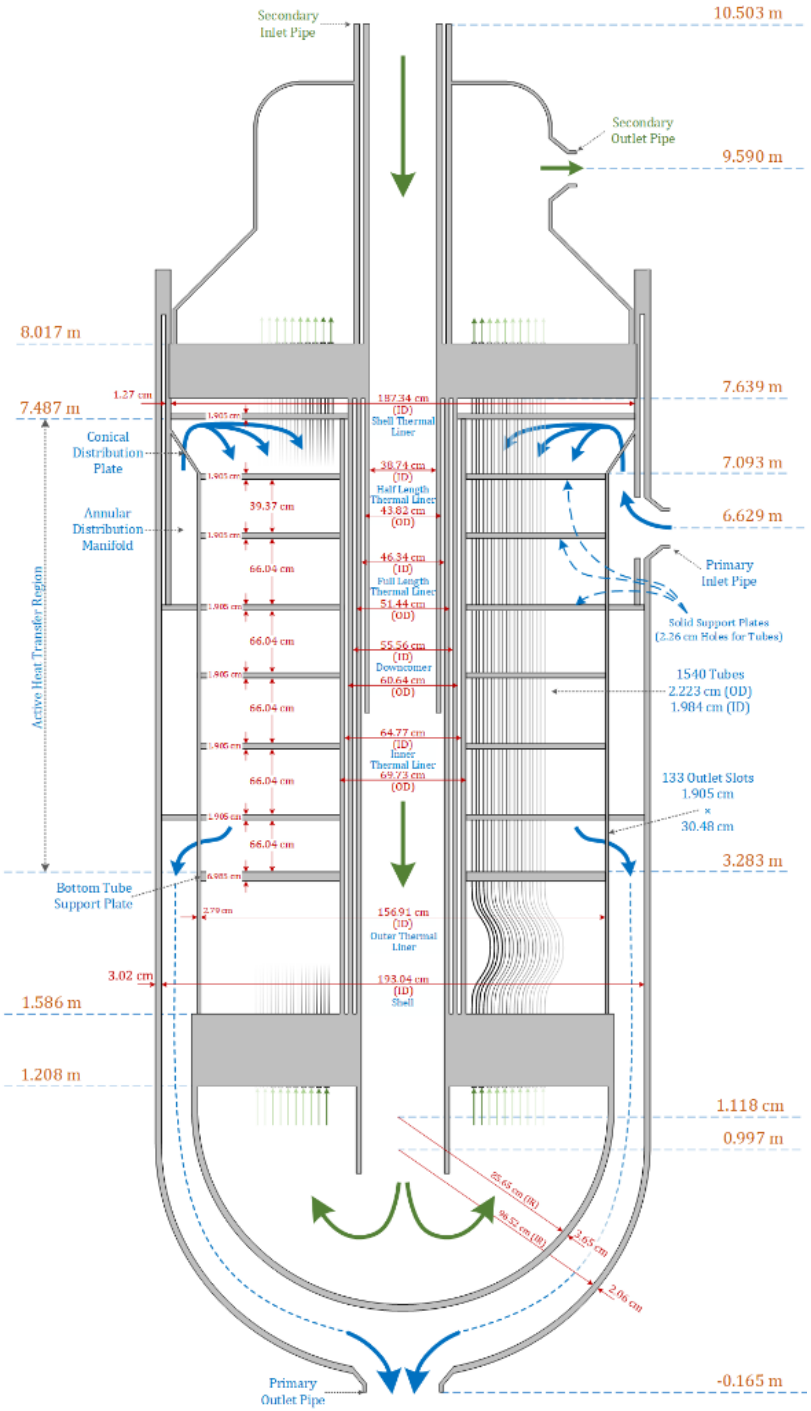

Figure 5. Schematic of the FFTF IHX. The primary coolant flow path is shown in blue while the secondary sodium flow path is shown in green. Elevations relative to the bottom of the core active region are shown in orange. Reprinted with permission. [2]

A secondary coolant loop provided cooling for each of the primary coolant loops. The heat generated in the reactor core was transferred to the secondary loops through the IHX and removed to the environment via four dump heat exchangers (DHX). Similar to the primary loop, each secondary coolant loop had a flow rate of roughly 734 kg/s.

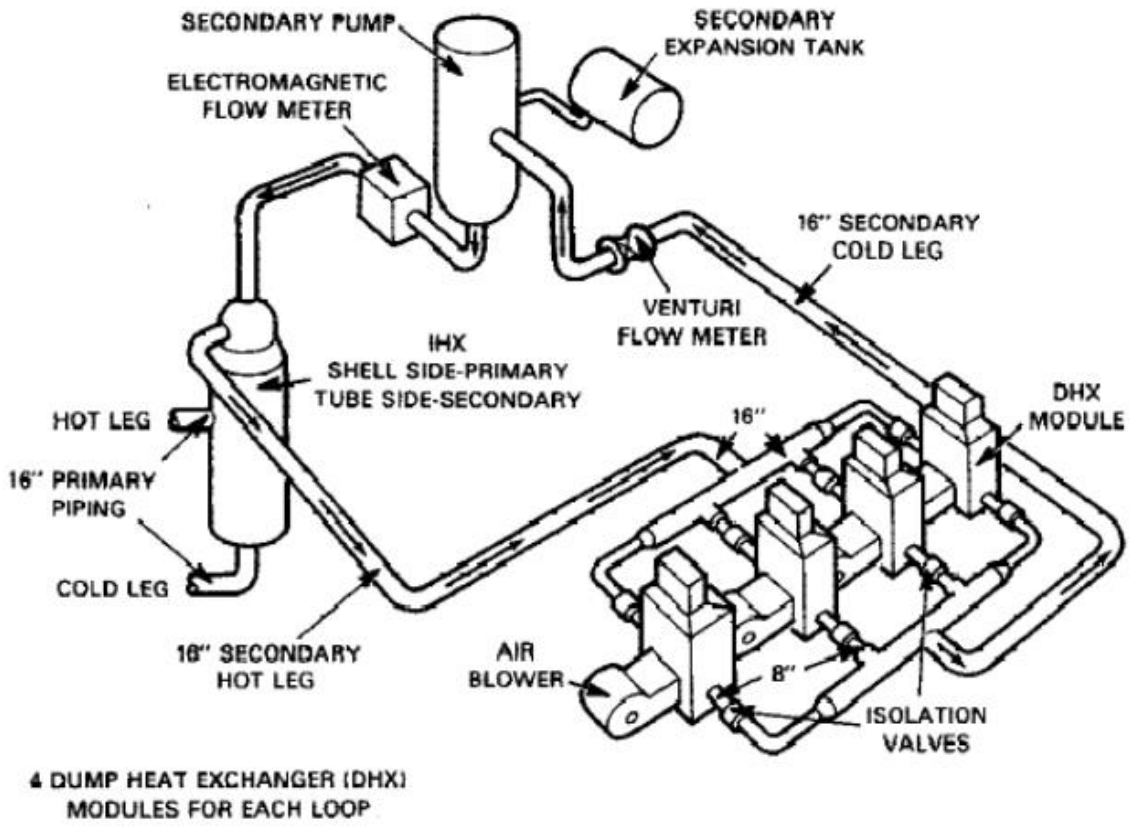

Figure 6. FFTF Secondary Coolant loop. Reprinted with permission. [2]

4. THE SYSTEM ANALYSIS MODULE

The code chosen for the analysis of the FFTF was the System Analysis Module (SAM), a system thermal hydraulic (STH) code currently under development at Argonne National Laboratory under the DoE's Nuclear Energy Modeling and Simulation program [3]. For the goals of the benchmark exercise, STH codes like SAM are ideal given their ability to model full reactor systems with relatively low detail, and thus, low computational costs compared to other types of thermal hydraulic analysis tools. While a variety of STH codes exist that are capable of modeling SFRs including RELAP5-3D and SAS4A/SASSYS-1, SAM was chosen because it offers a range of advantages over these codes [4,5].

A major motivation for using SAM to perform this benchmark is the support it is getting from the DoE, the US Nuclear Regulatory Commission, and the advanced nuclear reactor industry as a whole. Since its development began, SAM has become an increasingly common tool for advanced reactor analysis, and has performed a range of benchmarks demonstrating its efficacy. A successful benchmark using SAM has been completed on the air-cooled Natural Shutdown heat removal Test Facility, demonstrating the ability of SAM to model natural circulation driven systems [6]. Another successful benchmark has been completed using SAM to model the inherent safety features of the EBR-II, showing the ability of SAM to model pool type SFR designs [7]. SAM is also being used to support the development of commercial advanced reactors and expected to be utilized by the U.S. Nuclear Regulatory Commission for licensing commercial SFR designs. [8]

Performing safety analysis of sodium fast reactors (SFRs) is a primary motivation for developing SAM, so the creation of SFR relevant geometries is made straightforward by the code. A number of component types that involve the creation of multiple coupled fluid and solid domains can be created with a single input block. These components serve to both reduce the time required to generate input files, as well as to make SAM less prone to user errors. Examples of available components in SAM are ducted core assemblies, hexagonal assembly arrays, liquid volumes with cover gasses, and intermediate heat exchangers.

SAM also has a number of advanced capabilities that make it a valuable tool for advanced reactor analysis. These include the ability to create pseudo three-dimensional models where multiple one-dimensional and two-dimensional components can be coupled in a three-dimensional layout. This permits the analysis of complex systems where multi-dimensional effects are significant including SFR cores. A multi-dimensional flow model is also currently being developed for the purpose of modeling thermal mixing and stratification. This is useful for modeling large volumes where these effects play a significant role. Demonstrations have been done to couple SAM with CFD codes (STAR-CCM+ and Nek5000) and nuclear fuels codes (BISON) with other coupling projects planned. Using SAM a part of multi-physics/multi-scale simulations is major asset for the design and licensing of advanced reactors.

SAM has shown it is capable of modeling systems similar to the FFTF and it is believed the experienced gained using SAM for this benchmark will be valuable given

its current and projected relevancy. These factors indicate that SAM is an ideal tool for the analysis of the FFTF LOFWOS transient.

At the most basic level, SAM components are divided into three types: one-dimensional fluid components, two-dimensional heat structures, and zero-dimensional branches. One-dimensional fluid components are the dominant component type. These components solve one-dimensional versions of the mass, momentum, and energy conservation equations [9]. Empirical correlations based on component geometry and flow conditions are utilized to estimate the frictional loss coefficient and the heat transfer coefficient.

Heat structures are two-dimensional bodies typically coupled to one-dimensional fluid components to model solid objects like fuel assemblies or pipe walls. To model the heat transferred between heat structures and their coupled one-dimensional fluid components, the volumetric heat addition term is found using equation 1.

$$q''' = h(T_w - T)\frac{P_{heated}}{A_c} \quad (1)$$

Where:

q''' is volumetric heat addition

h is convective heat transfer coefficient

T_w is wall temperature

P_{heated} is the heated perimeter

A_c is coolant area

At their axial boundaries, one-dimensional fluid components can be connected to other fluid components via zero-dimensional branches. In their simplest form, zero-dimensional branches only need the outlet of one fluid component and the inlet of another to be specified. K-loss factors can be applied to calculate the pressure drop across these components. Equation 2 shows how the pressure drop in branches is calculated.

$$\Delta P_{form} = \frac{1}{2} K (\rho u^2)_{pipe} \qquad 2$$

Where:

ΔP_{form} is the form pressure loss

K is the form loss coefficient

ρ is the pipe fluid density

u is the pipe fluid velocity

Pumps are modeled as a special type of zero-dimensional branch where the pressure head is used as the pressure rise across the branch. Zero-dimensional branches can be modeled with a volume parameter allowing them to model transient, inertial, effects. Pressure boundary conditions can be applied to zero-dimensional volume branches as well. This feature is useful for modeling cover gas components where an ambient pressure is exerted on the liquid volume.

An alternative to connecting one-dimensional fluid components with branches is to explicitly state their boundary conditions with time dependent junction or time dependent volume boundaries. In time dependent junctions, the boundary velocity and temperature are specified while time dependent volumes specify the boundary pressure

and temperature. It should be noted that time dependent junctions are typically used as inlet boundary conditions and time dependent junctions are typically used as outlets. In this case, the temperature applied at the outlet is only used by the code in the case of a flow reversal. The next section of this document describes how these basic component types were used to create a model of the FFTF.

5. MODEL DEVELOPMENT – STEADY STATE

The success of using SAM to predict conditions in the FFTF during the LOFWOS transient will rely on the ability of the model to accurately capture the appropriate physical phenomena in each of the reactor's components. The first step of modeling the transient is to be able to accurately represent the initial steady state condition of the reactor with a SAM model. Experimental data was provided giving the reactors steady state operating conditions. This data was used to fine-tune the SAM model until a satisfactory agreement was found.

To better isolate the phenomena in the reactor and ensure each component SAM models faithfully represents its physical counterpart, the FFTF was divided into three main sections:

- Reactor vessel (RV)
- Intermediate heat exchanger (IHX)
- Primary loop piping.

Each of these independent sections, referred to as "open models" due to their open boundary conditions, were tested using boundary conditions derived from the steady state facility data to tune model parameters. Once each open model produced satisfactory results, they were combined to form a closed model representing the full FFTF. With a full model of the FFTF complete, it was then possible to apply the boundary conditions for the LOFWOS transient to create predictions for the parameters

of interest. The following sections provide details on the approaches and methods used to generate the individual models of the regions of the FFTF.

5.1. Reactor Vessel

A primary goal for the RV model was to ensure the flow distribution through each RV component was consistent with the benchmark specifications. This was achieved by tuning the K loss coefficients in the inlet and outlet plena. The components modeled within the RV included the following:

- Inlet plenum
- Core assemblies
- Additional flow paths
- Outlet Plenum

5.1.1. Inlet Plenum

The inlet plenum connected the primary loop outlets to each of the sixteen flow paths used to model RV components. In the SAM model, the inlet plenum was modeled as a zero-dimensional volume branch. To simplify the model, the inlet plenum also included the annular and peripheral plena adjacent to the core basket. Figure 7 shows how the flow paths described by the benchmark were simplified by the SAM model. This simplification is not believed to have a significant impact on the ability of the SAM model to predict the parameters of interest in the benchmark. By combining the multiple flow paths in the inlet plenum into simplified paths, the multiple assumptions that would have been needed to directly model the inlet plenum can be combined into one

representative parameter; namely, the K-loss coefficient between the inlet plenum and component inlet.

5.1.2. Core Assemblies

Of the sixteen flow paths used in the SAM model to represent RV components, thirteen represented core assemblies. Figure 8 shows the FFTF core and how it was divided for the SAM model. Generally, each core component in the SAM model represents one ring of the FFTF core. Exceptions were made for specially instrumented assemblies, which were modeled individually, and for the control, safety, and test assemblies, which were all grouped together regardless of their position in the core. Additionally, the outer two reflector rings were grouped into one SAM component. Between the thirteen modeled core assemblies, ten were modeled as fueled assemblies and three were modeled as reflector assemblies. The GEM assemblies were not included directly in SAM's thermal hydraulic model of the FFTF, however their reactivity feedback was included in SAM's point kinetics model.

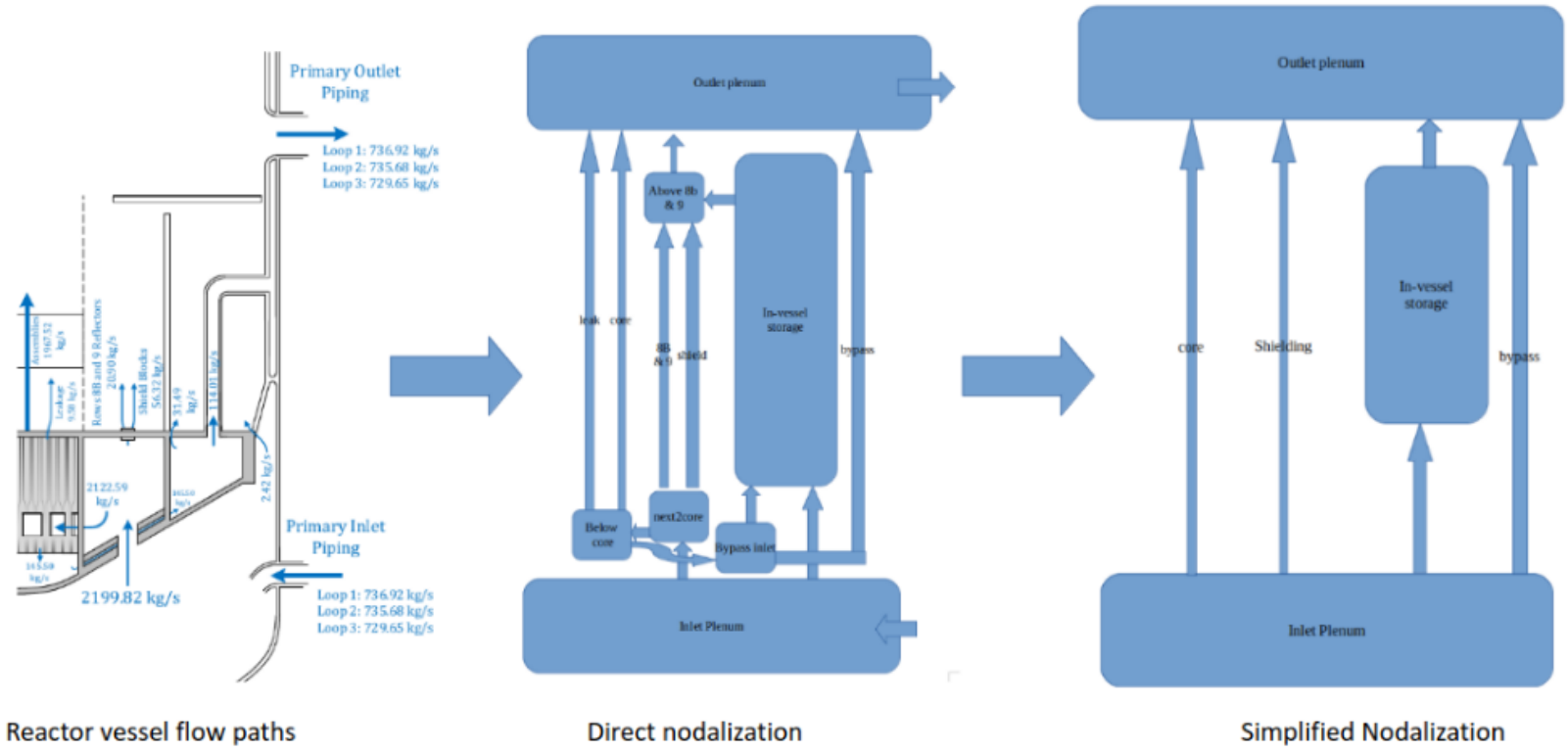

Figure 7. Scheme used to simplify the Inlet Plenum flow paths. Modified with permission. [2]

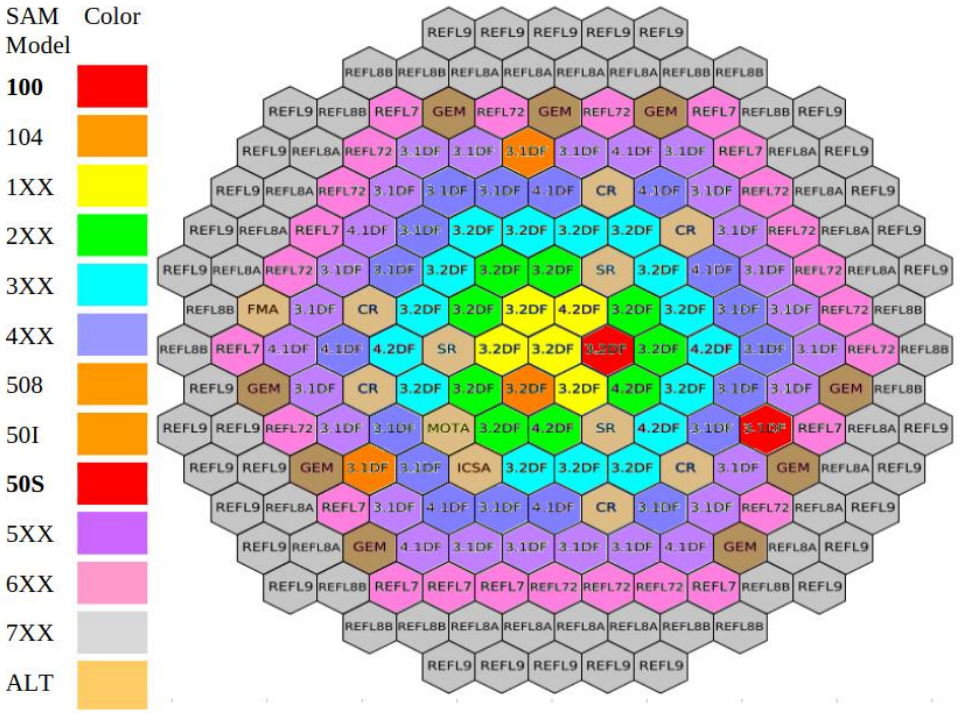

Figure 8. Division of FFTF core assemblies into SAM components. Fast response PIOTA assemblies are shown in red. Modified with permission. [2]

For each assembly type, the initial flow rate was given. These flow rates are shown in Table 1. The axial power distribution for each assembly was also provided, as determined by an Argonne National Laboratory neutronics analysis of the FFTF done to accompany the benchmark.

Table 1. Core Assembly flow rates

Assembly Type	# of Assemblies	Flow Per Assembly (kg/s)
3.2 Drivers	22	25.391
3.1 Drivers, Row 5	12	24.144
3.1 Drivers, Row 6	22	20.821
4.1 and 4.2 Drivers, Rows 2-5	12	25.389
4.1 Drivers, Row 6	5	19.968
3.2 Drivers with PIOTA, Rows 2,4	4	24.851
3.1 Drivers with PIOTA, Rows 6	3	20.500
MOTA	1	1.787
ICSA	1	2.043
Control and Safety Rods	9	4.545
FMA	1	0.650
Type 1, Row 7 Reflector	11	1.787
Type 2, Row 7 Reflector	15	0.891
Row 8a Reflector	24	0.728
Row 8b Reflector	18	0.529
Row 9 Reflector	30	0.379

The neutronics analysis also contained information regarding various reactivity feedbacks. These feedbacks included the effects of core expansion, fuel density changes, structure density changes, sodium density changes, the Doppler Effect, and the GEMs.

SAM contains a point reactor kinetic model which allows the power in selected components to be determined by designated reactivity feedbacks. While it is possible to implement all of the reactivity feedbacks provided by the benchmark into SAM, it was assumed that the GEMs would be the dominant reactivity feedback so they were the only feedback mechanism implemented into the model. The benchmark provided a correlation relating the sodium flow rate through the core to the GEM sodium level. The Argonne neutronics calculations provided a correlation between the GEM sodium level and the GEM reactivity. A combination of these correlations, plotted in Figure 9, was implemented into the SAM model.

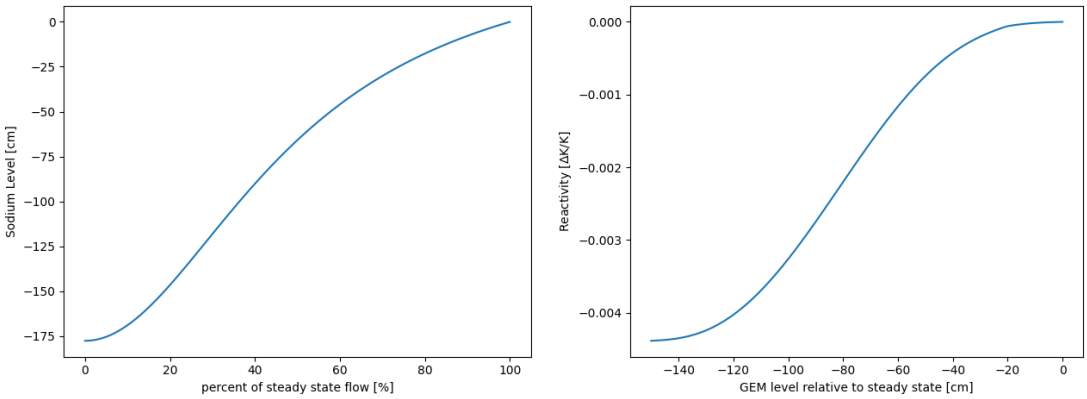

Figure 9. GEM correlations

5.1.2.1. Fuel Assemblies

The inner six rings of the FFTF core were primarily driver fuel assemblies. The axial profile of these assemblies, shown in Figure 10, consisted of a lower shield orifice, and a pin bundle region. Within the pin bundle cladding were four axial regions: the

lower reflector region, the active fuel region, the upper reflector region, and an upper fission gas plenum. Each assembly was surrounded by a stainless steel duct. Five of the fuel assemblies were Proximity Instrumented Open Test Assemblies (PIOTA). These assemblies were geometrically identical from other fuel assemblies, other than thermocouples located near the assembly outlet. Two of the PIOTAs, assemblies 100 and 50S, contained fast response RTDs. These PIOTAs produced results made available in the benchmark. Each of the five PIOTA assemblies were modeled individually in the SAM model.

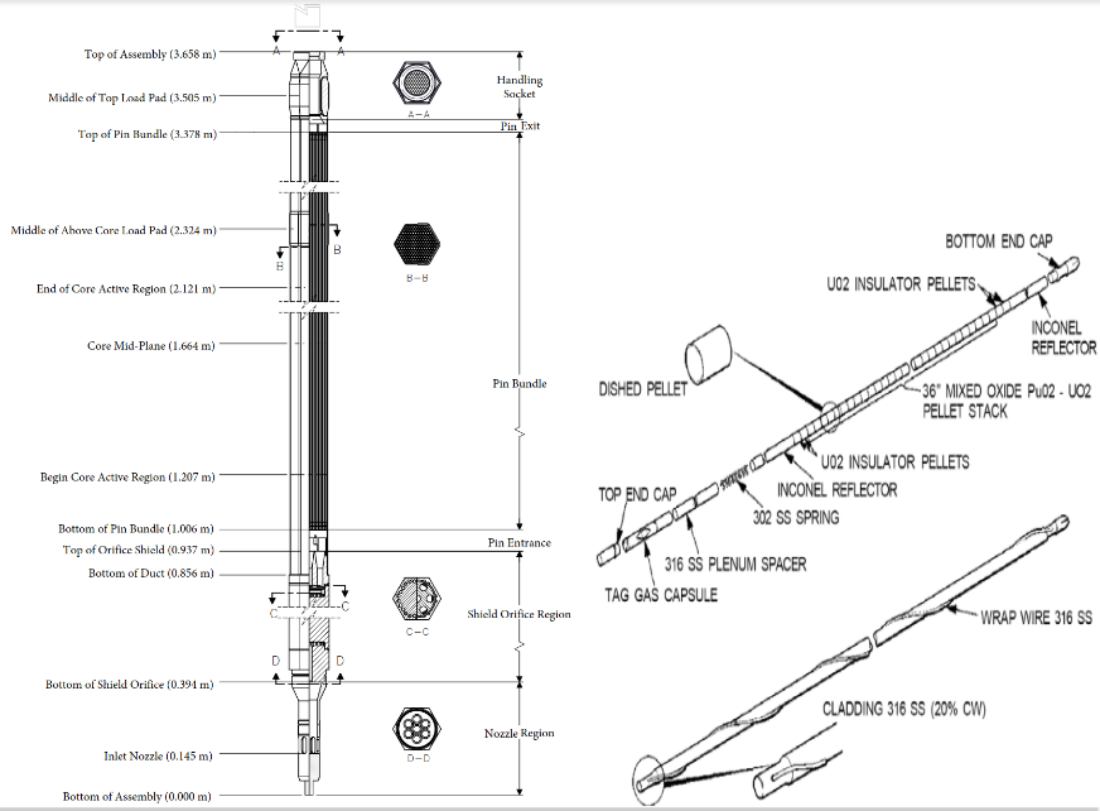

Figure 10. Left: Axial layout of a fueled assembly. Right: Individual fuel pin components. Reprinted with permission. [2]

Because orifice dimensions differed between assemblies, and to simplify the model, the orifice region was not directly modeled. Instead, the pressure drop effect of this region was captured by the K-loss factor applied between the inlet plenum and the fuel assembly. Each of the pin bundle regions was modeled by SAM's "PBDuctedCoreComponent". These components automatically create a one-dimensional fluid component coupled with a heat structure to represent the pin cladding and its internals. A second heat structure is added to model the assembly duct. With only one fluid component and one pin heat structure modeling each assembly, the results produced will represent the conditions for the average pin in the assembly. Given that the PIOTA thermocouples are near the assembly outlet, far from the heated section of the assembly, it is expected that the temperature will be homogenized before it is measured, making the pin averaging approach sufficient for predicting the experimental data provided in the benchmark.

The nodalization of the SAM fuel assembly model is shown in Figure 11. The axial element density in the reflector regions is much higher than other regions to help reduce instabilities caused by the temperature gradient in the fuel region. The effect of increasing the element density on reducing the magnitude of the instability is shown in Figure 13. The fueled region of the core assembly was modeled with 47 axial elements. At the top and bottom of the fueled region, there was a 2.03 cm long insulator pellet of natural or depleted uranium. Using 47 axial elements, the length of each element was 2.03 cm. The fission gas plenum was modeled with only 5 elements. Because this region is far from the heated region, the temperature gradients expected in this region will be

less severe, and thus requires a lower element density to accurately model. A similar philosophy was used to determine the number of radial nodes used in the heat structures. With larger temperature gradients expected in the fueled region, 9 elements were used to model the fuel, 1 element was used for the gap, and 3 were used for the cladding. In other regions, the cladding and gap were modeled with 1 element and the interior region was modeled with 3 elements. In all sections, the assembly duct was modeled with 1 radial element.

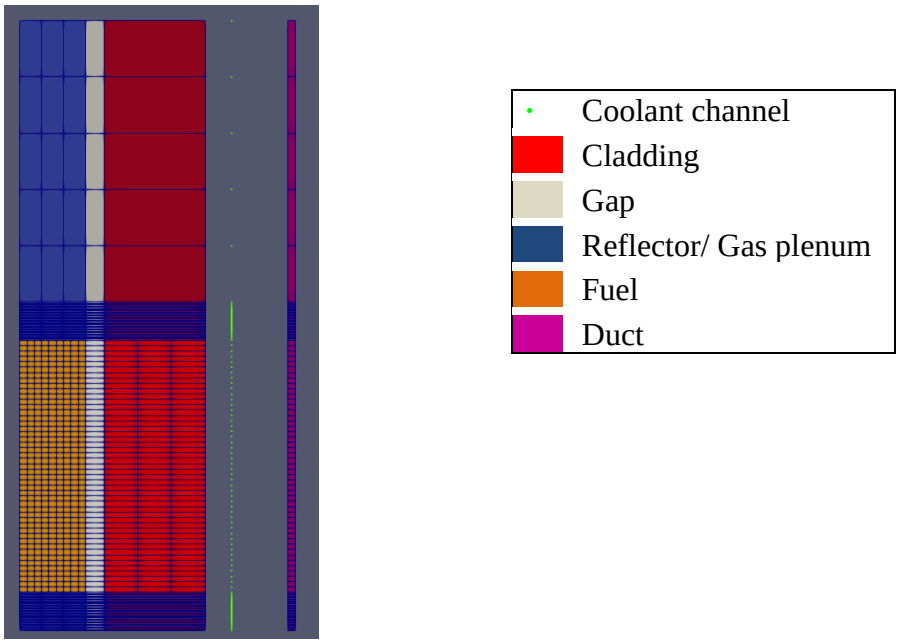

Figure 11. SAM model nodalization of the fuel assemblies (not to scale).

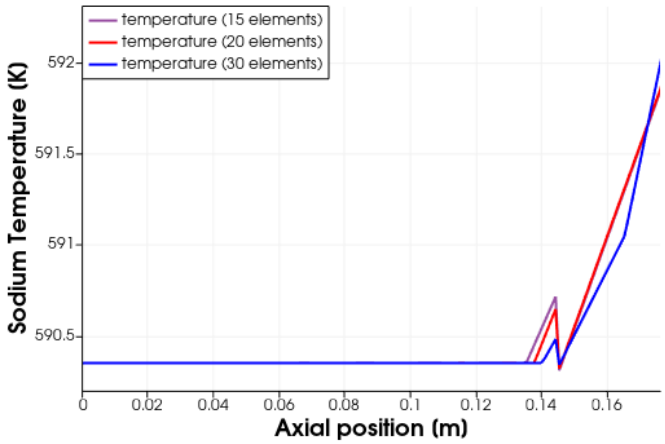

Figure 12. Effect of reflector elements on temperature instability.

The convective coupling between the heat structures and the fluid components was implemented using a rod bundle correlation for the heat transfer coefficient. By specifying a rod bundle geometry in the SAM input, the Updated Calamai / Kazimi-Carelli (1976) heat transfer correlation is utilized [10]. Additionally, the heat transfer surface area density is specified in the input to ensure the appropriate value for P_{heated}/A_c is used in Equation 1. Similar to the heat transfer coefficient, the friction factor is also found using a geometry specific correlation. By specifying a wire-wrapped geometry in the SAM input, the Cheng-Todreas (1986) correlation for friction loss is used [11].

The cladding and duct material was stainless steel-316. SS-316 was also used as the structural component in the fission gas plenum. Limited details were provided for the geometry of this region, so it was assumed to be composed entirely of SS-316 in the SAM model. The upper and lower reflector regions were composed of Inconel 600. The fuel used in the reactor was a mixture of UO_2 and PuO_2. Properties for each of these

materials were taken from a reference of theromphysical properties produced by the International Atomic Energy Agency [12]. The properties for the gap were derived from a reference provided by the benchmark. This reference provided a number of different correlations predicting wide range of values for the gap conductance. The average value of these correlations was used in the SAM model, but this value has a large uncertainty.

5.1.2.2. Reflector Assemblies

The three outer rings of the FFTF core primarily consisted of reflector assemblies. The axial profiles of these assemblies is shown in Figure 13. Unlike the fuel assemblies, coolant flows through channels within these assemblies rather than around wire wrapped pin bundles. The cross sections of these assemblies are shown in Figure 14. To simplify the model, the inner reflector ring was modeled with one component and the outer two rings were modeled as a second. This was based on the assumption that the inner ring, being closer to the active fuel region, would play a more important role than the outer rings.

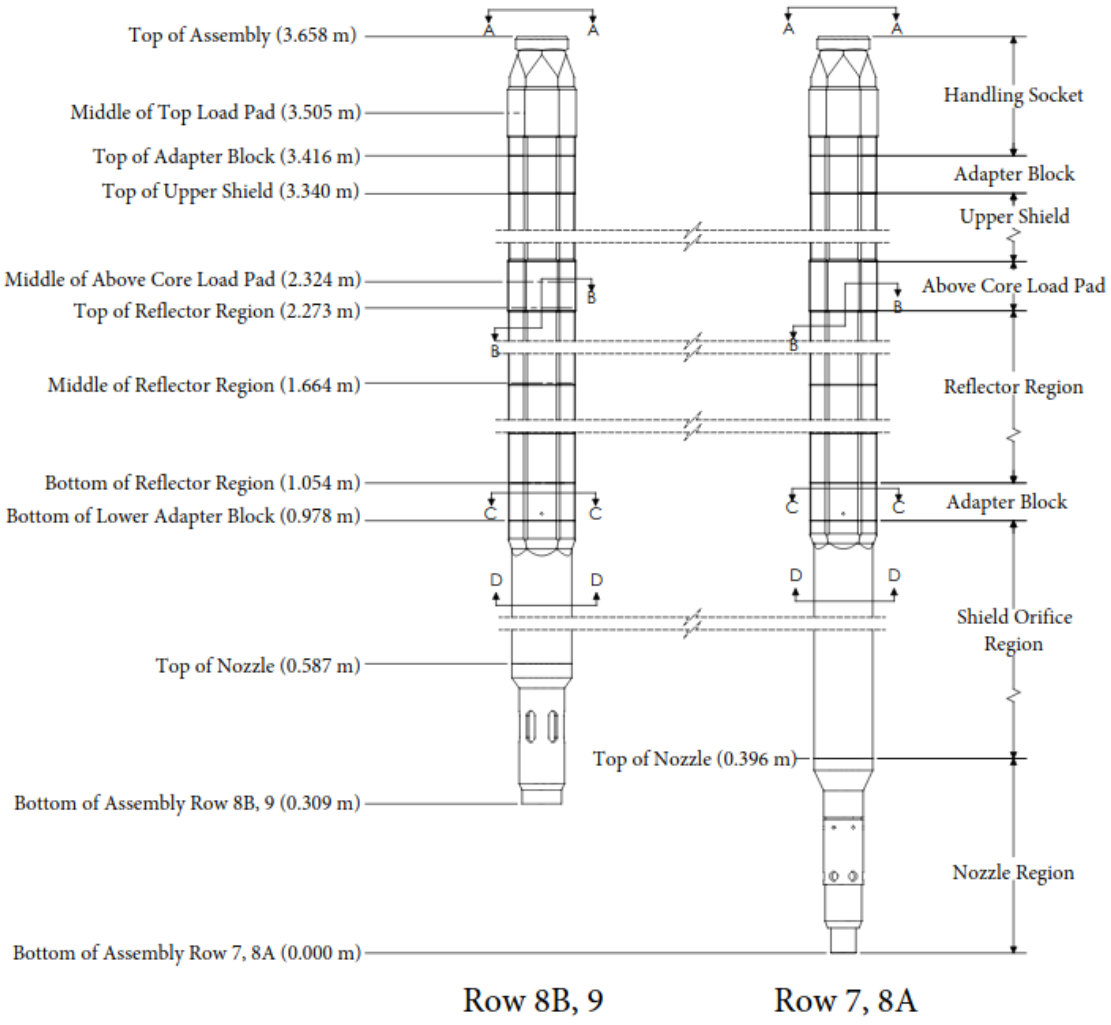

Figure 13. Axial profile of the reflector assemblies. Reprinted with permission. [2]

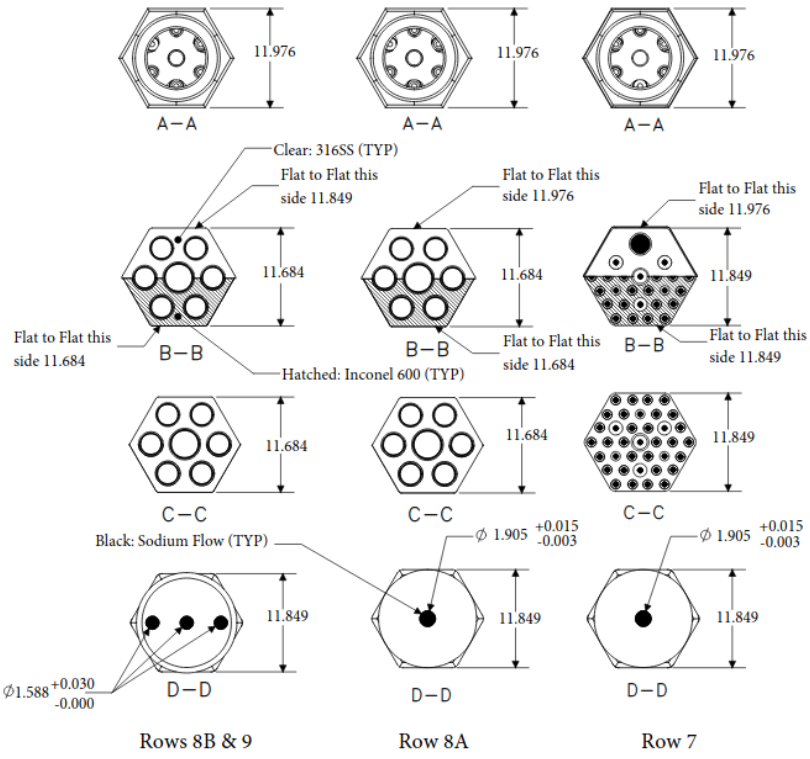

Figure 14. Cross sectional profiles of the reflector assemblies. Reprinted with permission. [2]

The SAM component modeling the outer two rings represented assemblies with different geometries. To accommodate this, the SAM model uses an averaged geometric representation of the reflectors. The SAM nodalization of the FFTF reflectors is shown in Figure 15. Unlike the fuel assemblies, the orifice region was modeled in the reflector assemblies. The reflector assemblies had a much lower flow rate than the fuel assemblies, so the orifice region was included to increase the reflector inlet velocity and decrease the necessary K-loss factor needed to achieve the correct pressure drop in the assembly. The nodalization of the ALT assembly used to model the control, safety, and

test assemblies is identical to the reflector nodalization, with the geometric parameters updated to reflect the average of the grouped assemblies.

Figure 15. SAM model nodalization of the reflector assemblies (not to scale).

5.1.2.3. Additional Flow Paths

Three of the sixteen RV components in the SAM model represent components where flow bypassed the reactor core. These components and the flow rates through them are shown in Figure 16.

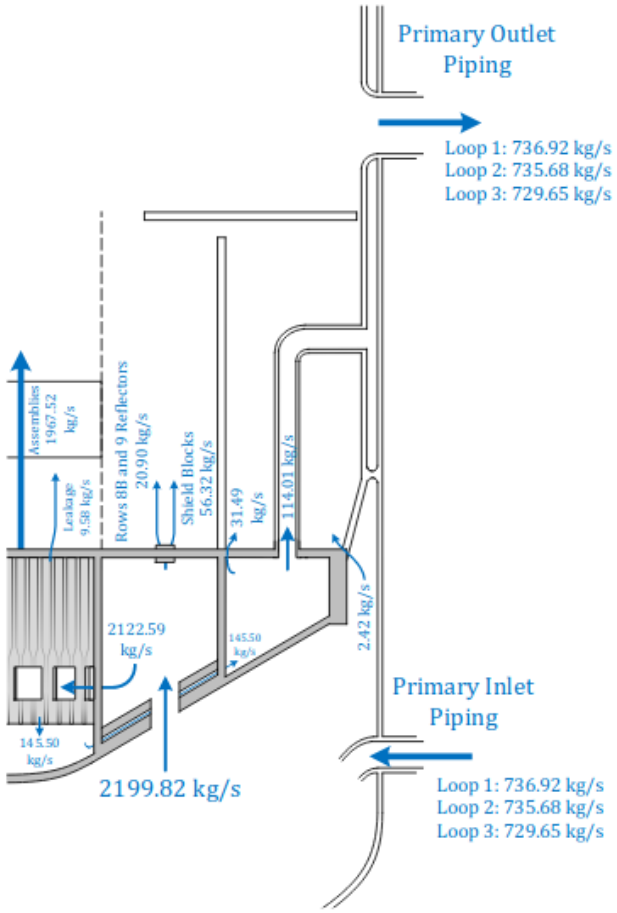

Figure 16. Flow distribution in RV. Reprinted with permission. [2]

The first of these components was the radial shield. Shown in Figure 17, this component consisted of plates of stainless steel to shield the reactor vessel from radiation escaping the reactor core. The sodium that flowed in this region was modeled with two one-dimensional fluid components, one representing the open region below the shield and second representing the region flowing through the shield. No heat structures were used to model the solid structures in this region based on the assumption that

temperature changes outside of the core, and thus the heat capacity of these components would not significantly impact the parameters of interest during the transient.

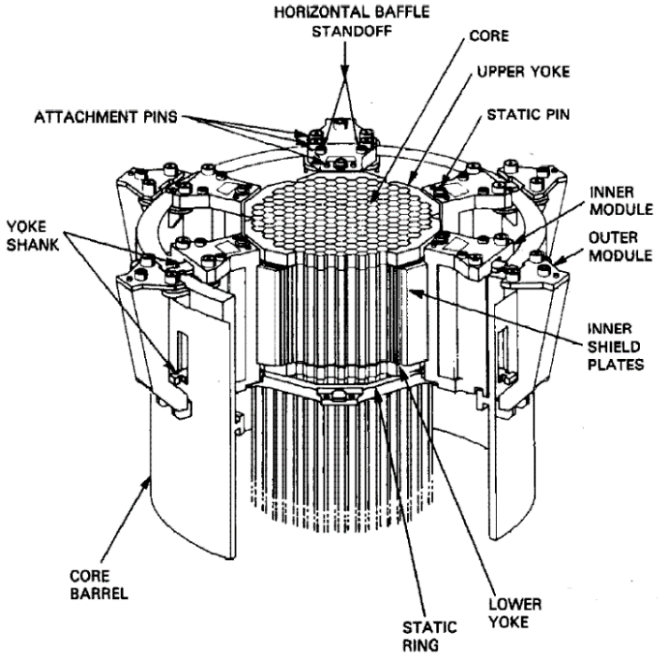

Figure 17. Drawing of the core support and radial shield. Reprinted with permission. [2]

Three core bypass channels in the reactor vessel directed sodium from the inlet plenum through an annular region around the RV wall before being expelled to the outlet plenum. This annular region provided cooling for the reactor vessel walls. Three one-dimensional fluid components were used to model this bypass path: one for the vertical portion of the annular region's inlet piping, one for the horizontal portion of the annular region's inlet piping, and one for the region lining the reactor vessel.

The final pathway connecting the inlet and outlet plenum was through the inner vessel storage region. Limited details were given for this component, and it was stated in

the benchmark documentation that this region is expected to have a minimal impact on the LOFWOS transient. This region was modeled with a single one-dimensional fluid component.

5.1.3. Outlet Plenum

The outlet plenum connected all the RV components with the inlets to the three primary coolant loops. It was modeled in SAM using a "PBLiquidVolume" component. This component creates a zero-dimensional volume branch. It also includes an ambient pressure condition to account for the argon cover gas in the RV. The pressure of the liquid component is determined by the ambient pressure and the liquid level of the component. While an initial liquid level is specified in SAM input, this level will change to respond to the pressure at the interface between the liquid volume and the connected fluid components. In the open RV model, a short outlet component was used with the outlet plenum connected to its inlet and a pressure condition applied at its outlet. This pressure condition was set so that the sodium level in the outlet plenum was consistent with the level specified in the benchmark.

5.1.4. Steady State RV Model

To check the consistency of the RV model with the FFTF steady state conditions provided in the benchmark, two parameters were considered: the flow rate through each RV component and the pressure drop across the RV. Both of these parameters depend heavily on the K-factors applied between the inlet and outlet plena and the other RV components. In the benchmark documentation, the expected pressure drop across various reactor components was calculated. The results relevant to the RV are shown in Table 2.

Table 2. RV Pressure Drops

Component	Calculated pressure drop [kPa]
RV Inlet Pipe to Core Basket	57.2
Core Basket to Outlet Plenum	733.6
Outlet Plenum to RV Outlet Pipe	4.8

The K factors needed to match the pressure drops between the plena and the coolant loop piping were found using Equation 2. Finding the correct K factors needed for the internal RV components was more complicated because the pressure drops depended on both the form loss from the K-loss factor and the frictional losses within the components. To calculate the necessary K-loss factors, an open model was created for each internal RV component. The inlet and outlet conditions of these models were measured, and Bernoulli's equation, shown in Equation 3, was used to determine the pressure drop across the component at the benchmark specified flow rate.

$$P_1 + \frac{1}{2}\rho u_1^2 + \rho g h_1 = P_2 + \frac{1}{2}\rho u_2^2 + \rho g h_2 + \Delta P_{friction} \quad 3$$

Where:

P is pressure

ρ is fluid density

u is fluid velocity

h is elevation

$P_{friciton}$ is the frictional pressure loss

To avoid calculating the gravitational term, ρgh, which is not straightforward when the fluid density changes due to heating, the orientation of the model was changed such that the axial dimension was perpendicular to the gravity vector. With the frictional losses now known, the K factor required to generate the total pressure drop across the component can be found using Equation 2. By matching the pressure drop across all components at their desired flow rates, the flow rate in each component will remain the same when all components are combined in a single model. To verify this, RV component flow rates from the SAM model are compared with the benchmark specified values in Table 3. With all of SAM's predicted flow rates within a 1.5% relative error to the benchmark value, and most errors well below 1%, these results were considered satisfactory.

Table 3. Comparison of SAM steady state RV conditions to benchmark values

Component	Benchmark flow [kg/s]	SAM flow [kg/s]	Error
100	25.48	25.38	0.28%
104	25.46	25.36	0.29%
1XX	127.3	127.0	0.28%
2XX	229.2	228.5	0.29%
3XX	407.5	406.3	0.30%
4XX	443.2	442.1	0.27%
508	20.9	20.82	0.12%
50I	20.9	20.82	0.13%
50S	558.6	20.82	0.13%
5XX	32.9	557.9	0.51%
7XX	38.9	33.02	1.49%
ALTXX	45.3	38.36	-0.14%
Radial Shield	56.8	56.32	0.84%
Bypass	114.9	114.0	0.78%
Storage	34.2	33.9	0.84%

5.2. Coolant Loops

Although the three coolant loops were geometrically identical, they were modeled independently to accommodate their slightly different initial and boundary conditions for the LOFWOS transient. Loops 1, 2, and 3 had initial flow rates of 736.91 kg/s, 735.68 kg/s, and 729.65 kg/s respectively. The boundary conditions for each loop included the pump speed, and the fluid conditions on the secondary side of the IHX.

5.2.1. Intermediate Heat Exchanger and Secondary Loop

The IHX was modeled using SAM's PBHeatExchanger component. This component automatically creates two one-dimensional fluid components with a single heat structure coupled to both. The secondary side of the IHX consisted of over 1500 tubes. These were all represented by the single one-dimensional fluid component in the IHX model. Zero-dimensional volume branches were used to model the inlet and outlet region of the IHX. A representation of the IHX model in SAM is shown in Figure 18.

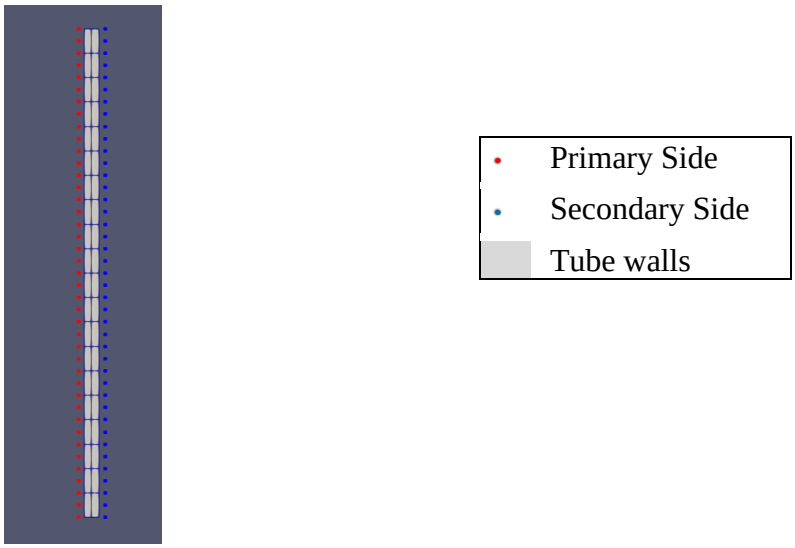

Figure 18. SAM nodalization of the IHX

The tube side of each IHX was part of the secondary sodium coolant loop.. The outlet temperature of each DHX was provided in the benchmark, as was the total mass flow rate of each secondary loop. With these boundary conditions, the secondary loops were modeled as an open system in the SAM model. Because the mass flow rate through

each DHX was not provided, it was assumed that the total secondary loop flow rate was divided evenly between each. With the mass flow rate provided for the entire LOFWOS transient, modeling the secondary pump was not necessary. This made considering the pressure loss effects in the secondary loop unnecessary as well. An arbitrary pressure outlet of 100 kPa was applied at the IHX secondary side outlet. The section of the secondary loop represented in the SAM model is highlighted in Figure 19.

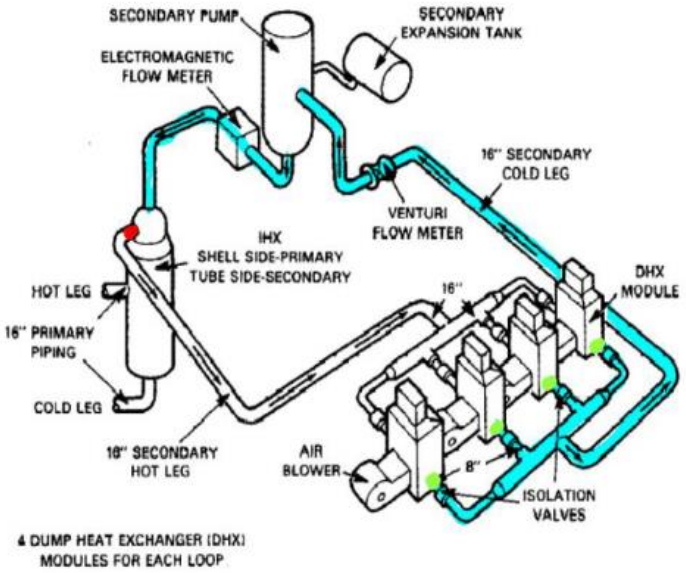

Figure 19. Schematic of the FFTF secondary coolant loop. Modified with permission. [2]

The initial secondary cold leg temperature was also provided in the benchmark. The RTDs responsible for this measurement were located between the electromagnetic flow meter (shown in Figure 19) and the IHX. It was expected that this temperature would be roughly the average of the DHX outlet, with a slight increase due to pump

heating effects. Instead, the secondary cold leg temperature was roughly 4°C below the average DHX outlet temperature of each loop. This discrepancy was cited as being due to “uncertainties and the location of the thermocouples within the DHX” in the benchmark documentation. With only the initial cold leg temperatures provided while the DHX outlet temperature response was given for the entire transient, no effort was made to correct for this discrepancy in the SAM model.

Two parameters were of concern when comparing the SAM model of the IHX to the benchmark specifications: the energy transfer between the primary and secondary loops, and the pressure drop across the primary side of the IHX. The energy transferred by the IHX must equal the total energy produced in the core. To test this, an open IHX model was created with the inlet temperature specified as the outlet temperature predicted in the open RV model, 660K. The average IHX outlet temperature between the three loops should equal the benchmark specified core inlet temperature of 590K. To account for the small differences between the boundary conditions in each of the three loops, the average boundary conditions were used in this model. The IHX temperature distribution is shown in Figure 20.

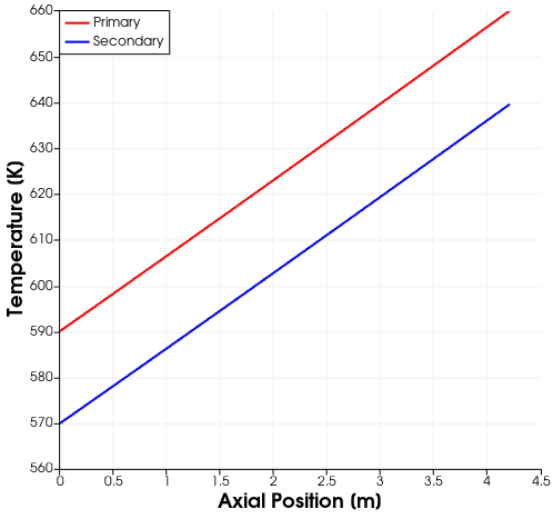

Figure 20. IHX steady state coolant temperatures

The energy transferred from the primary to the secondary loop is dependent on the thermal resistance in the IHX. Shown in its cylindrical form in Equation 4, the thermal resistance is a function of the IHX geometry, tube material properties, and the heat transfer coefficient on the primary and secondary sides.

$$Q_{IHX} = \frac{(T_1 - T_2)}{R_{IHX}} \tag{4a}$$

$$R_{IHX} = \frac{1}{h_1(2\pi r_1)L} + \frac{\ln(r_1/r_2)}{2\pi kL} + \frac{1}{h_2(2\pi r_2)L} \tag{4b}$$

Where:

Q_{IHX} is energy transferred from primary side to secondary side

T_1 is primary sodium temperature

T_2 is secondary sodium temperature

R_{IHX} is IHX thermal resistance

h_1 is primary side heat transfer coefficient

h_2 is secondary side heat transfer coefficient

r_1 is tube outer radius

r_2 is tube inner radius

L is IHX length

k is tube thermal conductivity

With the IHX geometry parameters fully described in the benchmark documentation, the only flexible variables in the model were the heat transfer coefficients. In SAM, the default heat transfer correlation can be used with a scaling factor to allow the model to be tuned to desired parameters. For the IHX, the Updated Calamai / Kazimi-Carelli (1976) tube bundle heat transfer correlation was used for the primary, shell side. The Seban-Shimazaki (1951) pipe geometry correlation was used to find the heat transfer coefficient on the secondary, tube side [13]. When the default, unscaled, heat transfer coefficients were tested in the SAM model, it was found that the IHX outlet temperature closely matched the desired core inlet temperature.

The benchmark provided a calculation result for the predicted pressure drop across the IHX of 57.9 kPa. To match this value, a K-loss factor was applied between the IHX inlet plenum and the primary loop pipe feeding into the IHX. Similar to the methodology used for the RV components, Equation 3 was used to find the frictional losses in the IHX, with a sideways oriented model used to negate gravitational effects.

5.2.2. Primary Loop Piping

The remaining portion of the FFTF model consisted of the piping that connected the RV and IHX. This piping including the primary sodium pumps. The benchmark documentation provided the geometric details of the piping as well the pressure losses across valves and piping in the primary loop. The primary loop was modeled using a combination of one-dimensional fluid components representing straight sections of pipe and zero-dimensional volume branches representing elbows and other bends. Heat structures representing pipe walls were omitted with the assumption that their effect on the parameters of interest would be negligible during the transient. Additionally, the heat losses from the piping to the environment was neglected, as it was found insignificant in the steady state model. The number of elements used to model each section of straight pipe in the SAM model was determined by rounding the length of the pipe up to the nearest integer value, then multiplying that value by five. Figure 21 shows the SAM representation of the primary loop, including the heat exchanger.

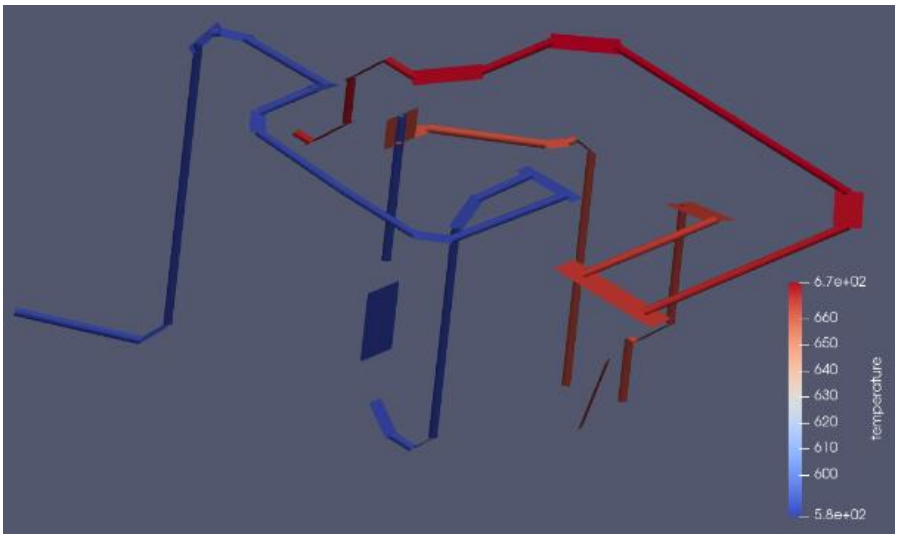

Figure 21. SAM model of the primary coolant loop

When comparing the primary loop model with the steady state benchmark specifications, matching the pressure drops was a primary consideration. To account for the pressure losses in valve components, zero-dimensional, zero-volume branches were added where these valves connected to the primary loop piping. The K-loss factors applied to these valves were found using Equation 2.

In the straight sections of pipe, the default SAM correlation for frictional losses in pipe geometries was used. For turbulent flow regimes, this was the Blasius-McAdams correlation [14]. For the elbows and bends, a K-loss factor was applied so that the total pressure drop in the primary loop matched the values given in Table 4. The same K-loss was used for all elbows, and double that value was used for “U” and “S” shaped bends in the piping.

Table 4. Primary Piping pressure losses

Component	Calculated pressure drop [kPa]
Hot and Cold Leg Piping (total)	85.5
Hot Leg Isolation Valve	0.62
Cold leg Isolation Valve	9.7
Check Valve	62.7

5.2.3. Primary Pump

The SAM model for the pump consisted of a "PBPump" component and a one-dimensional fluid component representing the pump cavity. SAM's PBPump component is a zero-dimensional, volume-less branch where the pump head can be specified as a constant value or using a function. In the benchmark documentation, a pump curve was provided, shown in Equation 5. This curve was implemented directly into the model by coupling the pump head function with post processors for the mass flow rate and fluid density in the pump. A second function was created for the pump speed. For steady state simulations this function was constant, using the benchmark specified steady state pump speed. A conditional statement was added to the pump curve so that a negative pressure head occurred when the pump speed dropped below 1 RPM. The value of the pressure loss was dependent on the flow rate through the pump.

$$\bar{H} = (\bar{N}^2 + \bar{Q}^2) W_h(\bar{Q}/\bar{N}) \quad (5a)$$

$$W_h = \sum_{i=0}^{6} a_{h,i}[\pi + \arctan(\bar{Q}/\bar{N})]^i \quad (5b)$$

Where:

$\bar{H}$ is dimensionless pump head

$\bar{N}$ is dimensionless pump speed

$\bar{Q}$ is relative volumetric flow rate

$a_{h,i}$ are pump curve coefficients, shown in Table 5.

Table 5. Pump Curve Equation Coefficients

i	a_h
0	431.96699
1	-576.61438
2	301.00029
3	-75.465859
4	8.6754986
5	-0.26062352
6	-0.01596287

Dimensionless parameters were found by dividing model values by the following nominal values:

- Pump head: 152.4 m Na (566°C)
- Pump speed: 1110 rpm
- Volumetric flow rate: 0.9148 m^3/s

Using the steady state parameters shown in Table 6, it was found that the average pump head was 850 kPa. This value was unexpectedly low, given that the total pressure loss predicted by the benchmark calculations was 1020kPa. After discussion with the benchmark organizers, it was determined that the pressure loss calculations were overestimated and that the pressure head provided by the pump curve at the steady state conditions should be the trusted value. It was suggested by the benchmark organizers that the pressure drop in all components be reduced evenly, with an extra 5% reduction across the RV. This resulted in a 16% reduction being applied to the originally provided pressure losses (21% between the core basket and outlet plenum).

Table 6. LOFWOS Initial Pump Conditions

Parameter	Loop 1	Loop 2	Loop 3
Primary Pump Speed	953.1	951.5	944.4
Primary Loop Flow Rate	736.91	735.68	729.65

5.3. Full Model and Steady State results

After each of the open FFTF sections matched the steady state initial conditions, they were combined to create a full, closed loop model of the FFTF. It was found that SAM struggled to converge when simulating the closed loop model with best estimate initial conditions. To accommodate this, a full loop, open model was simulated by replacing the pump components with open boundary conditions. In this case, a velocity boundary condition was applied to both the inlet and outlet. Typically, applying a

velocity, or mass flow, boundary condition at two points in the same system will cause instability in the solver and should be avoided. However, the variable sodium level in the RV outlet plenum both allowed for small deviations in the overall conservation of mass between the system inlet and outlet, and created a pressure boundary condition so that system was fully defined. After results using the open, full loop model were obtained, the pumps were reintroduced and the full closed loop model was run with initial conditions taken from the previous simulation. For the initial, closed loop simulation, the pump head was calculated as the pressure difference between the inlet and outlet in the open simulation. Finally, after results were obtained from the closed loop, constant pump head model, the simulation was restarted using the new results as initial conditions with the benchmark specified pump curve used to determine the pump head. Table 7 shows a comparison between the closed loop, steady state conditions predicted by the SAM model, and the initial conditions of the LOFWOS transient provided by the benchmark. In all cases, the error between the SAM measurement and the benchmark value was within the uncertainty of FFTF instrumentation; specifically 2.8% for the primary loop flow rates and 1.5K for RTD temperature measurements.

Table 7. Comparison of SAM steady state predictions with benchmark values

Provided Parameter	Benchmark Value	SAM prediction	Error
Core inlet temperature [K]	590.4	591.6	0.20%
Mass Flow (loop 1) [kg/s]	736.91	736.55	-0.05%
Mass Flow (loop 2) [kg/s]	735.68	734.91	-0.10%
Mass Flow (loop 3) [kg/s]	729.65	728.18	-0.20%
Mass flow (total) [kg/s]	2202.24	2199.54	-0.12%
Core Flow Rate (total) [kg/s]	1998.00	1993.07	-0.25%
IVS Flow Rate [kg/s]	33.91	34.29	1.12%
Bypass Flow Rate [kg/s]	114.01	115.22	1.06%
Shield Flow Rate [kg/s]	56.32	56.95	1.12%

6. TRANSIENT MODEL

To predict the results of the LOFWOS transient, the FFTF SAM model was run using the steady state results as initial conditions and time dependent boundary conditions; namely:

1. Primary pump speed curves (provided by the benchmark)
2. Secondary loop flow rates (provided by the benchmark)
3. DHX outlet temperatures (provided by the benchmark)
4. Core power level (not provided by the benchmark)

Figures 22 to 24 show boundary conditions 1 through 3 over the course of the transient. These boundary conditions show that the secondary coolant loop is relatively unchanged during the transient. FFTF operators allowed the temperature of the DHX outlets to increase just before the pumps are tripped to help stabilize the temperature in the primary loop. The secondary loop flow rate was unchanged allowing the secondary loop to act as an effective heat sink for the primary coolant.

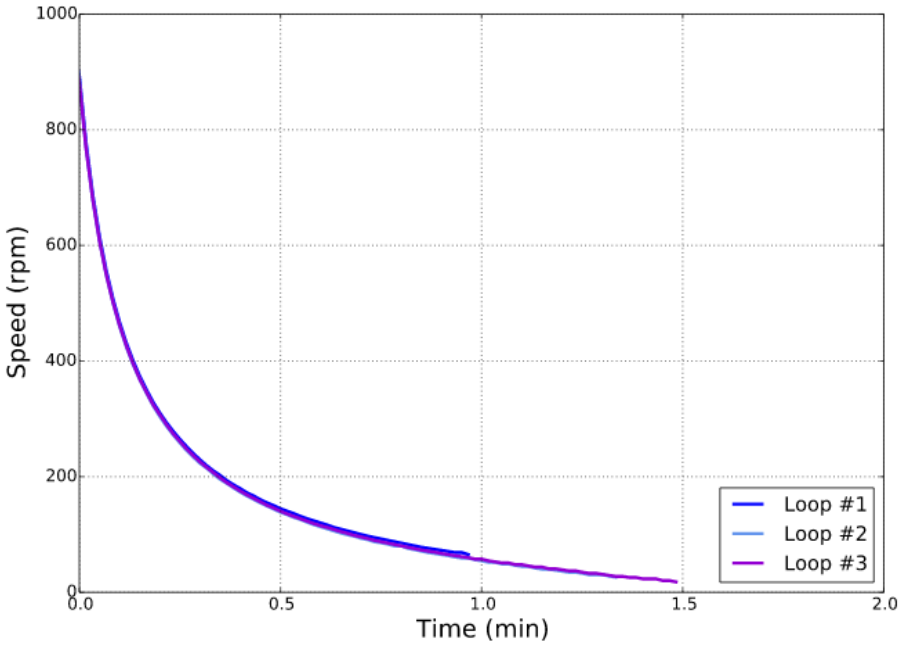

Figure 22. Primary pump coast down curves. Reprinted with permission. [2]

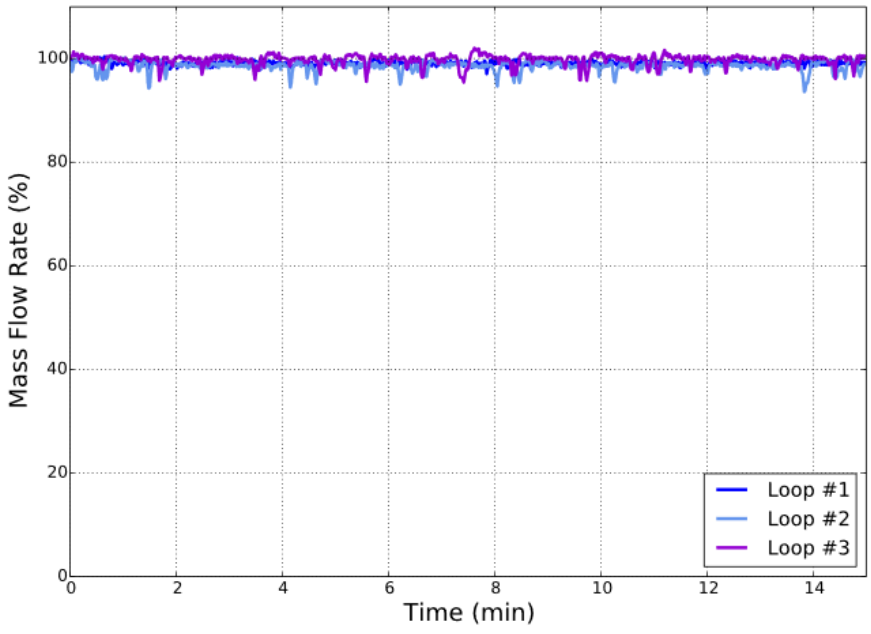

Figure 23. Secondary loop flow rate relative to initial condition. Reprinted with permission. [2]

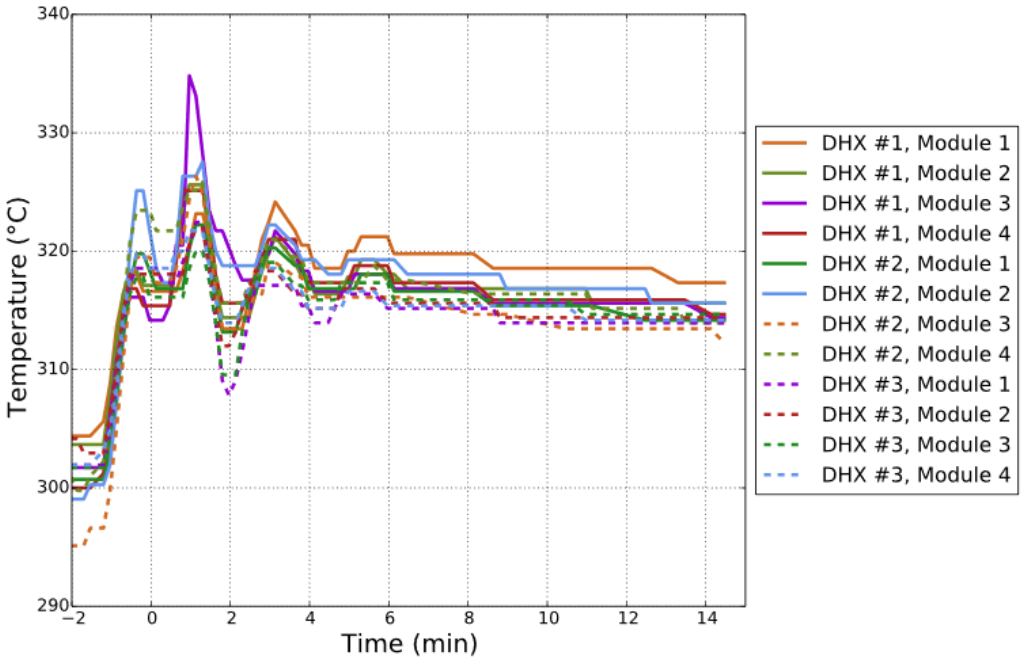

Figure 24. DHX outlet temperatures. Reprinted with permission. [2]

To define boundary condition 4, two factors needed to be considered: the change in fission power and the decay heat curve. Neither of these were provided by the benchmark. The change in fission power was modeled using SAM's point reactor kinetics model. As discussed previously, this model only accounted for the reactivity change effects from the GEMs. It was initially expected that a decay heat curve would be made available through the benchmark, however, this did not end up being the case. SAM currently does not have decay heat modeling capabilities, so the decay curve from a RELAP5-3D LWR model was used to estimate the FFTF decay curve [15].

There were a number of additional assumptions needed to justify using a model created by matching only steady state parameters for transient analysis. They are as follows:

1. Radial and axial power distributions will remain constant during the transition from fission as the dominant power source to decay heat as the dominant power source.
2. Heat losses to the environment remain insignificant
3. K loss factors remain constant for the range of flow regimes experienced during the transient
4. Coolant in the outlet plenum is well mixed before exiting to the primary coolant loop
5. Radial heat transfer between RV assemblies is not significant

7. RESULTS AND DISCUSSION

This section details the comparisons between the results obtained from the SAM simulations and the experimental results revealed at the end of the blind phase. With experimental results revealed, they could also be used to update the boundary conditions of the model in an effort to produce a more realistic simulation. The results presented in this section will be presented at the CRP's second Research Coordination Meeting [16].

7.1. Blind Phase Results

Figure 25 shows how SAM's prediction for the mass flow rate in the three primary coolant loops compares to the experimentally measured results. While, generally, the results show a good agreement, there were two main deviations. Early in the transient, it was observed that the mass flow rate predicted by SAM decreased slightly before the experiment. The cause of this difference has not been found and is a focus of continued investigation as the CRP continues. The second difference is between the low flow rates after the FFTF has transitioned to a quasi-steady state, natural circulation driven flow. This difference is believed to be caused by the difference between the experimental decay heat value and the decay heat curve implemented in SAM.

Figure 26 shows the results for the PIOTA outlet temperature predictions. In both the experimental results and SAM predictions, two peaks are observed. The early peak is caused by the power dropping slightly after the mass flow rate drops. The second peak is reached when an equilibrium between the decay heat generated in the core and natural

circulation heat removal is reached. This peak decreases later in the transient as the decay heat curve drops. The difference between the SAM and experimental results in the second peak is a result of a difference between the power level predicted by SAM during this period of the transient.

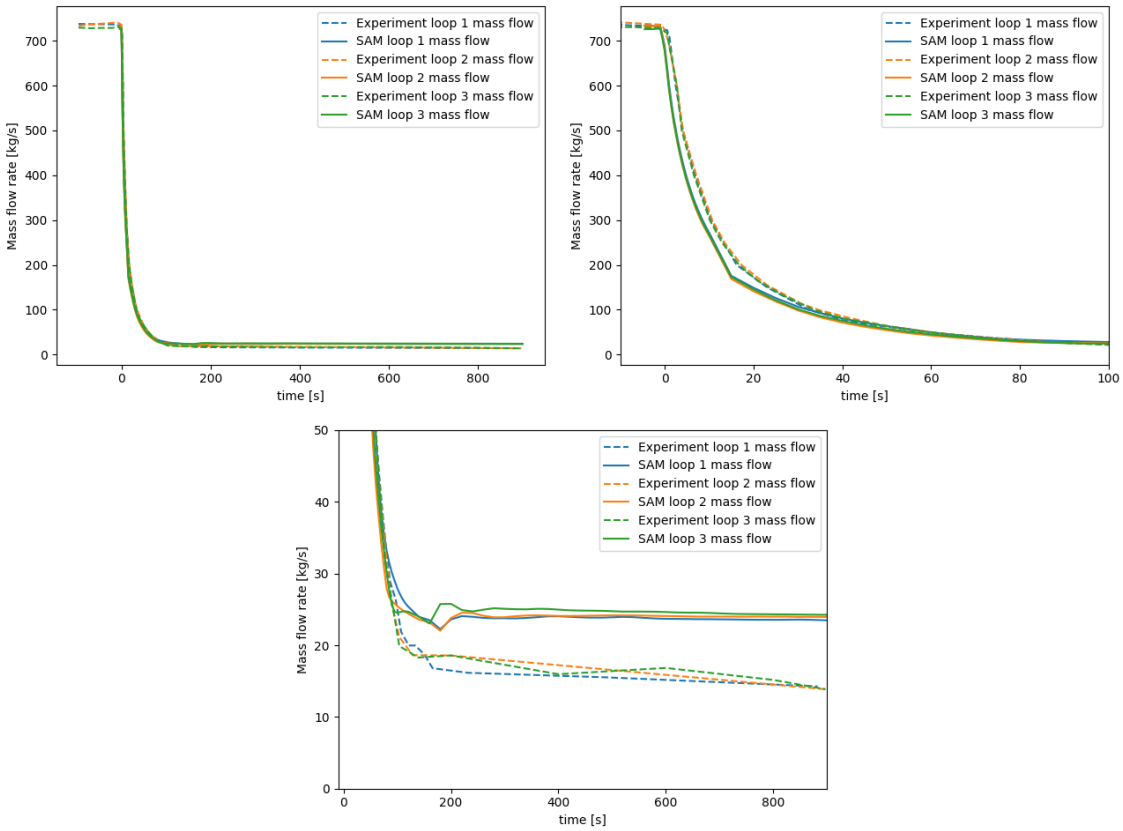

Figure 25. Comparison between SAM prediction and experimental mass flow rate.

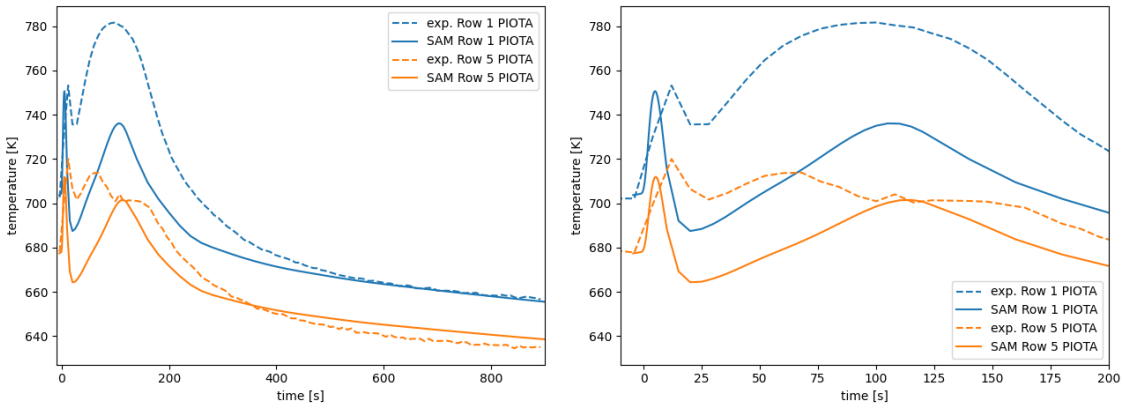

Figure 26. Comparison between SAM prediction and experimental PIOTA outlet temperatures.

Figure 27 shows the results for the coolant temperatures in the primary hot and cold legs. Interestingly, there was no significant temperature change observed in the hot leg, despite the temperature rising in the core outlet shown by the PIOTA results. This result is believed to be caused by the large sodium mass in the upper plenum and thermal mixing effects. With the lower mass flow rate after the pump trip, the thermal mixing in the upper plenum is expected to be reduced. This will result in the hotter coolant coming out of the core in the center of the outlet plenum having less of an opportunity to mix with the cooler coolant in other regions of the outlet plenum before leaving to the primary coolant loops. With SAM modeling the outlet plenum as a zero-dimensional volume, perfect thermal mixing is assumed. This is believed to explain the discrepancy between experimental results and SAM's prediction. The differences in the cold leg temperatures are believed to be a primarily a result of the measurement uncertainties in the DHX outlet temperature.

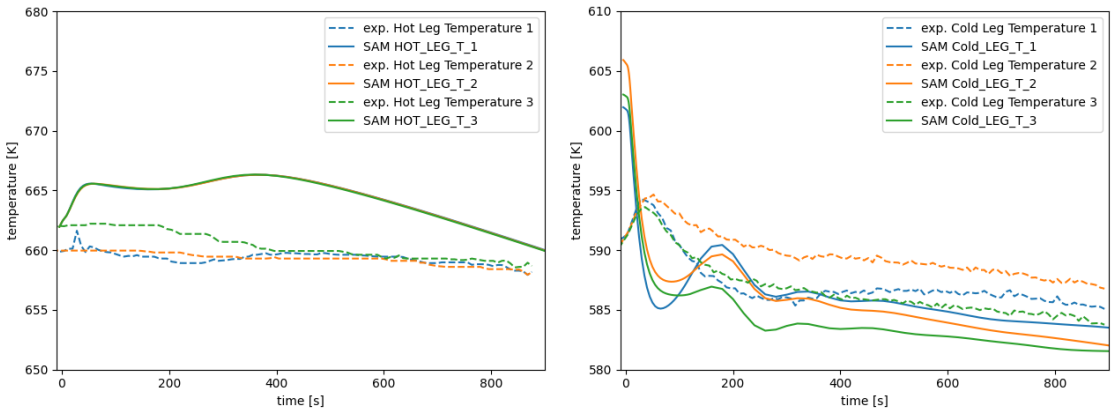

Figure 27. Comparison between SAM prediction and experimental primary loop hot and cold leg temperatures

Figure 28 shows the difference between the reactivity predicted by the SAM model and the reactivity determined from the experimental results. Both curves show a large drop early in the transient, however SAM over predicts this drop and fails to account for the rise in reactivity after about 100 seconds. These differences are caused by the assumption in the SAM model that the GEMs would be the dominant reactivity feedback for the duration of the transient. In reality, it is believed that the fuel Doppler effect and increased fuel density caused by the fuel rods cooling with less power generation were responsible for a significant positive reactivity feedback.

Figure 29 shows how both the reactivity and decay heat assumptions made in the SAM model affected the power level. Early in the transient when the fission power was still significant, SAM predicted a lower power level because of the reactivity assumptions made. Later in the transient SAM over predicted the power because of differences between the decay curve implemented in the model and the experimental decay curve.

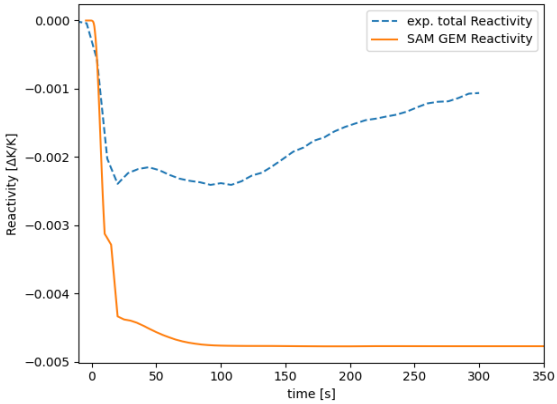

Figure 28. Comparison between SAM prediction and experimental reactivity.

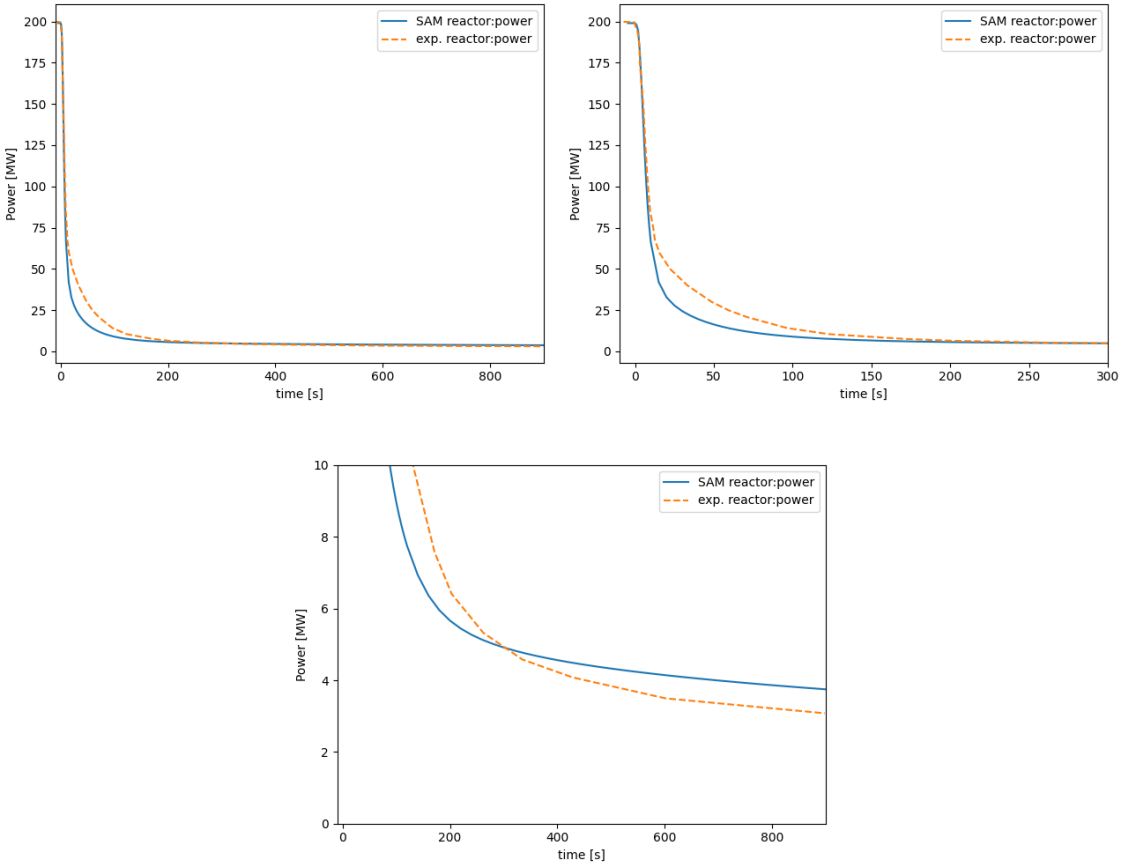

Figure 29. Comparison between SAM prediction and experimental power levels.

7.2. Updated Boundary Conditions

With the end of the blind phase, experimental results were made available to the benchmark participants. This allowed the SAM model to be run with updated boundary conditions that matched the experimental values. Specifically, the power level in the SAM model was updated to match experimental values, no longer relying on the point kinetic reactivity feedback model. Additionally, the secondary loop cold leg temperature was applied in place of the DHX outlet temperatures. The secondary cold leg temperature is shown in Figure 30.

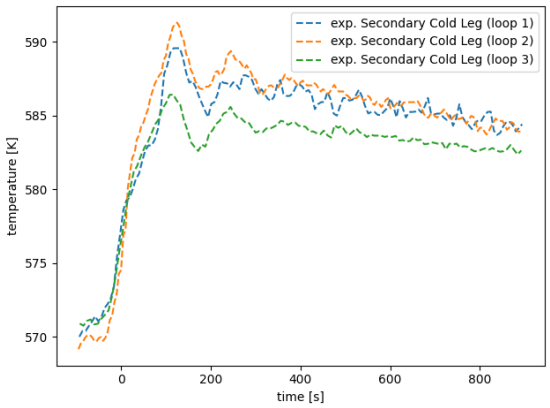

Figure 30. Experimental secondary cold leg temperatures

The updated results show a generally better agreement between the SAM and experimental results. The updated mass flow rate, shown in Figure 31, while still showing a deviation early in the transient, is better matched after natural circulation has been established. This confirms that the over prediction of the natural circulation flow shown in Figure 25 was largely caused by an over prediction of the decay heat.

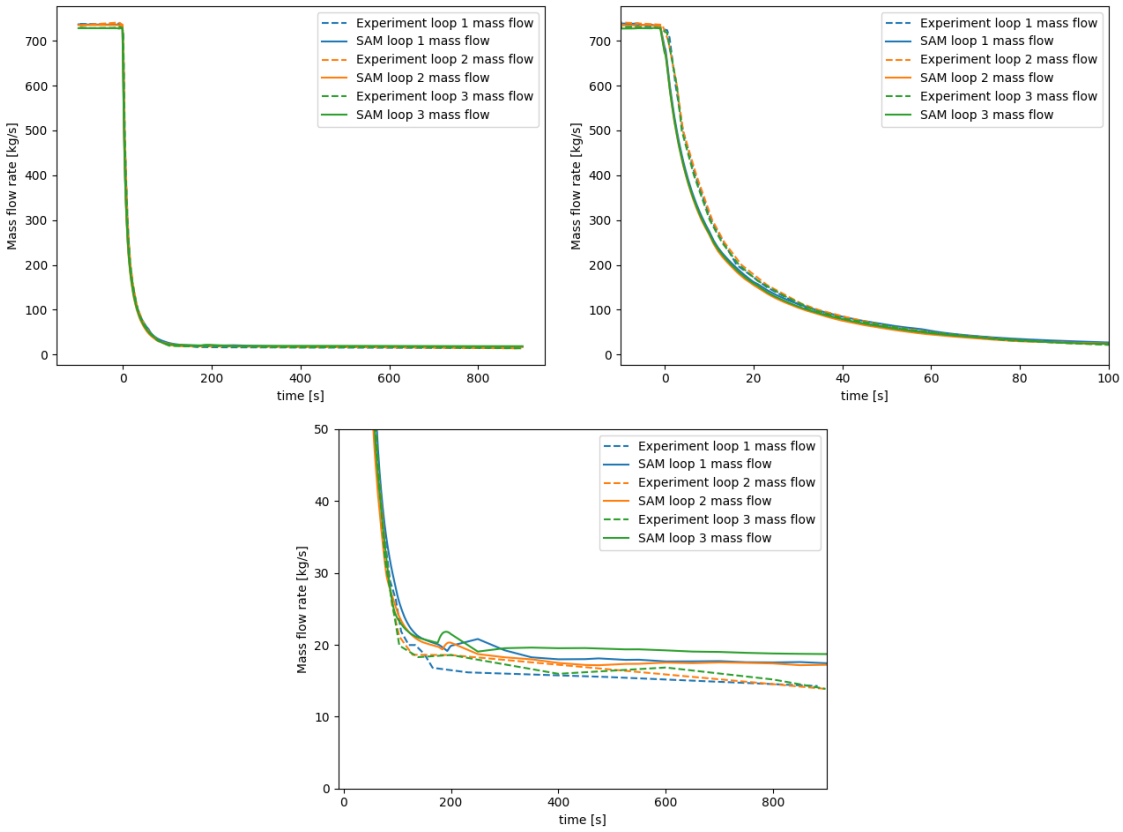

Figure 31. Comparison between SAM prediction and experimental mass flow rate with updated boundary conditions.

The row 2 PIOTA outlet temperatures, shown in Figure 32, show a better match with experimental results as well with results changing from under predicting the outlet temperature by 46°C to over predicting the outlet temperature by 24°C after implementing the new boundary conditions. The row 5 PIOTA response is more complex as SAM is showing a peak similar to the row 2 PIOTA with a lower magnitude while the experimental results show a much more flattened response. This difference is believed to be a result of not implementing radial heat transfer in the SAM model. A

shifting flow distribution in the core during the transient could also play a role in this result.

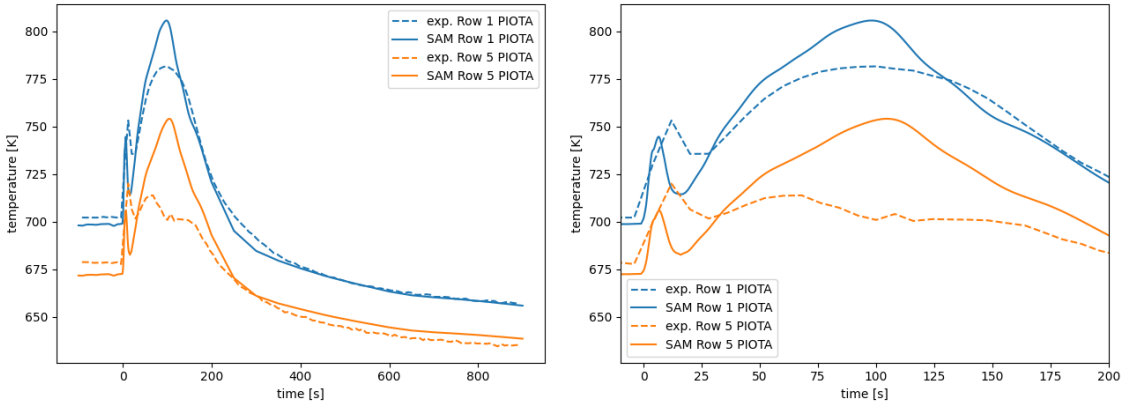

Figure 32. Comparison between SAM prediction and experimental PIOTA outlet temperatures with updated boundary conditions.

The updated SAM predictions for the hot and cold leg temperatures are shown in Figure 33. As expected, the hot leg temperature in the SAM model increased when the power level was increased early in the transient. This temperature remained higher later in the transient due to the reduced natural circulation mass flow rate. As shown in Figure 30, the secondary loop cold leg temperature was increased roughly 15°C during the first 200 seconds of the transient. This results in the primary cold leg temperatures increasing early in the transient in both the SAM and experimental results. However, after the pumps are tripped, SAM predicts the primary cold leg temperature will quickly drop to near the secondary loop temperature, then rise as the secondary temperature continues to rise. The experimental results show the cold leg temperature falls much more slowly,

coming to equilibrium with the secondary loop only after the secondary loop temperature has stabilized. This could be a result of neglecting to account for solid body heat capacities in the primary loop model.

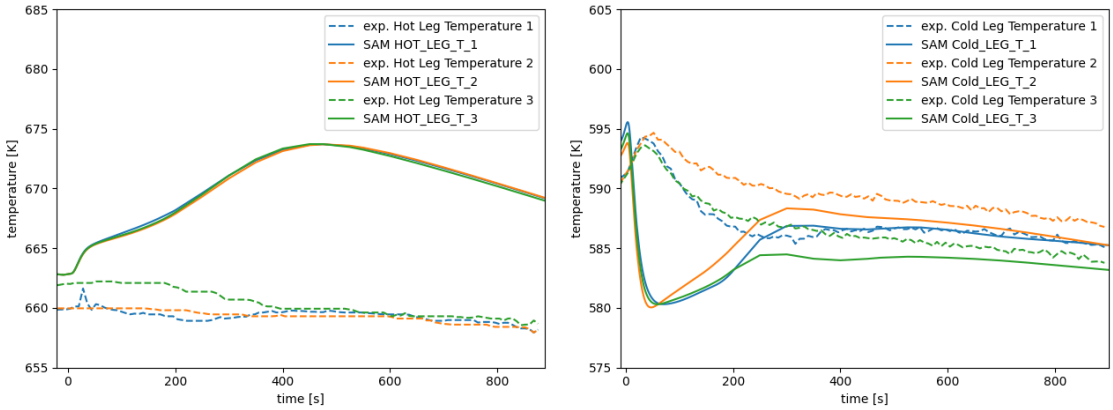

Figure 33 Comparison between SAM prediction and experimental primary hot and cold leg temperatures with updated boundary conditions.

8. CONCLUSIONS

The work presented in this thesis has shown that SAM is a capable tool for the analysis of the FFTF. With appropriate tuning applied to the facility model's K-losses, SAM was able to reproduce the conditions in the FFTF at the LOFWOS initial conditions within the accuracy of the facility instrumentation. A comparison between the SAM prediction of transient results and experimental values showed that FFTF reactivity feedback could not be accurately captured by only considering the GEMs. The cooling reactor core produces a significant positive reactivity feedback, slowing the fall of fission power. By applying the experimental transient power level to the SAM model, the prediction of the peak coolant core outlet temperature was improved to within 24°C. Other deviations in the SAM results were identified including the primary hot and cold leg temperatures and the ring 5 PIOTA outlet temperature. Potential causes for these deviations were identified and will be the focus of additional development of the model as the CRP progresses.

REFERENCES

[1] Benchmark Analysis of FFTF Loss of Flow Without Scram Test. IAEA, 20 Dec. 2017, www.iaea.org/projects/crp/i32011.

[2] Sumner, T., Moisseytsev, A., Heidet, F., Wootan, D.W., Casella, A.M., Nelson, J.V., Argonne National Laboratory, unpublished information, 2017.

[3] Hu, R., Zou, L., Hu, G., SAM User's Guide, Argonne National Laboratory, ANL/NSE-19/18, Argonne, IL, August 2019.

[4] INEEL-EXT-98-00834, RELAP5-3D Code Manual, Rev. 2.4.

[5] T. H. Fanning,ed., The SAS4A/SASSYS-1 Safety Analysis Code System, ANL/NE-12/4, Nuclear Engineering Division, Argonne National Laboratory, January 31, 2012.

[6] Hollrah, B., et. al. 2020. Benchmark Simulation of the Natural Convection Shutdown Heat Removal Test Facility Using SAM, Nuclear Technology 206, 1337-1350, 2020.

[7] Hu, R., Sumner T., Benchmark Simulations Of The Thermal-Hydraulic Responses During EBR-II Inherent Safety Tests Using Sam, Proceedings of the 2016 International Congress on Advances in Nuclear Power Plants, San Francisco, CA, April 2016, 1632-1641.

[8] U.S. Nuclear Regulatory Commission. NRC Non-Light Water Reactor (Non-LWR) Vision and Strategy, Volume 1, January 31, 2020.

[9] Hu R., SAM Theory Manual. Technical Report ANL/NE-17/4, Argonne National Laboratory, 2017.

[10] Kazimi M.S., Carelli M.D., Heat Transfer Correlation for Analysis of CRBRP Assemblies. Westinghouse, CRBRP-ARD-0034, 1976.

[11] Cheng S.K., Todreas N.E., Hydrodynamic models and correlations for bare and wire wrapped hexagonal rod bundles - bundle friction factors, subchannel friction factors and mixing parameters, Nuclear Engineering and Design 92, 227–251, 1986.

[12] International Atomic Energy Agency, Thermophysical Properties of Materials for Nuclear Engineering: A Tutorial and Collection of Data, IAEA, Vienna, 2009.

[13] Seban R.A., Shimazaki T.T., Heat transfer to a fluid flowing turbulently in a smooth pipe with walls at constant temperature. Transactions of the ASME, Vol. 73, 803-809, 1951.

[14] Todreas N.E., Kazimi M.S., Nuclear Systems. Volume 1: Thermal Hydraulic Fundamentals - Second Edition, CRC Press, Taylor & Francis Group, 1986.

[15] Vaghetto R., Hassan Y.A., Study of debris-generated core blockage scenarios during loss of coolant accidents using RELAP5-3D, Nuclear Engineering and Design 261, 144-155, 2013.

[16] Hollrah B., Vaghetto R., Hassan Y.A., Simulation Of The Fast Flux Test Facility Loss-Of-Flow Without Scram Accident Scenario Using The Sam Computer Code (Blind Phase), Presentation submitted to 2nd RCM of the IAEA CRP I31032 on Benchmark Analysis of Fast Flux Test Facility (FFTF) Loss of Flow Without Scram Test, Vienna, Austria, February 2021.